



8-2020

Advanced Analysis of Plutonium: Pre- and Post-Detonation Scenarios

Jessica L. Bishop
University of Tennessee, jbisho25@vols.utk.edu

Follow this and additional works at: https://trace.tennessee.edu/utk_graddiss

Recommended Citation

Bishop, Jessica L., "Advanced Analysis of Plutonium: Pre- and Post-Detonation Scenarios. " PhD diss., University of Tennessee, 2020.
https://trace.tennessee.edu/utk_graddiss/6791

This Dissertation is brought to you for free and open access by the Graduate School at TRACE: Tennessee Research and Creative Exchange. It has been accepted for inclusion in Doctoral Dissertations by an authorized administrator of TRACE: Tennessee Research and Creative Exchange. For more information, please contact trace@utk.edu.

To the Graduate Council:

I am submitting herewith a dissertation written by Jessica L. Bishop entitled "Advanced Analysis of Plutonium: Pre- and Post-Detonation Scenarios." I have examined the final electronic copy of this dissertation for form and content and recommend that it be accepted in partial fulfillment of the requirements for the degree of Doctor of Philosophy, with a major in Nuclear Engineering.

Maik Lang, Major Professor

We have read this dissertation and recommend its acceptance:

John D. Auxier, Lawrence Heilbronn, Ning Xu, Ania Szykiewics

Accepted for the Council:

Dixie L. Thompson

Vice Provost and Dean of the Graduate School

(Original signatures are on file with official student records.)

**Advanced Analysis of Plutonium: Pre- and Post-Detonation Scenarios
(LA-UR-20-25250)**

A Dissertation Presented for the
Doctor of Philosophy
Degree
The University of Tennessee, Knoxville

Jessica Lyn Bishop

August 2020

Copyright © 2020 by Jessica Lyn Bishop

All Rights Reserved.

DEDICATION

To my dog, Higgs

ACKNOWLEDGEMENT

This work was supported immensely by numerous individuals, most notably my adviser Maik Lang, who gracefully accepted me as a graduate student despite me having just spent over 3 months living on my bicycle. Thank you for believing in me. I also owe our greater research group both present and alumni including Igor Gussev, Eric O’Quinn, Will Cureton, Ryan Unger, Raul Palomares, Devon Drey, Irfan Ibrahim, Patrick Huston, and Alex Solomon. Thank you all for your support, guidance, and friendship. There are a variety of instrument scientists who have been invaluable in my data interpretation such as Miguel Crespillo, Anthony Faiia, Michael Koehler, and John Dunlap who I appreciate for their patience and enthusiasm in collaboration. To all of my LANL affiliates – Samuel Clegg, Beth Judge, Dana Labotka - I am grateful for your flexibility and eagerness to assist me. Thank you Ania Syznkiewicz for all of your honest advice and encouragement and Lawrence Heilbronn for your instruction and kindness. Last, my LANL mentors – John D. Auxier II and Ning Xu - I cannot thank you enough for welcoming me so warmly and for your commitment to my academic success. I truly appreciate you all.

This work was supported by the U.S. Department of Homeland Security (DHS) Domestic Nuclear Detection Office (DNDO) Academic Research Initiative (ARI) under Grant 2015-DN- 077-ARI093. The views presented in this paper are those of the authors do not necessarily reflect those of U.S. Dept. of Homeland Security (DHS), DNDO, or the ARI. This material is also based upon work supported under an Integrated University Program Graduate Fellowship. Any opinions, findings, conclusions or recommendations expressed in this publication are those of the author(s) and do not necessarily reflect the views of the Department of Energy Office of Nuclear Energy.

ABSTRACT

There is a significant gap in scientific knowledge as to how nuclear reactions in surface environment lead to distinctive chemical and isotopic signatures that are not present in nature, especially for nuclear forensics purposes. The aim of this research was to improve nuclear forensics capabilities, offering insight to rarely linked characterization methods (i.e. IRMS and Raman spectroscopy), in the scope of a plutonium-based nuclear weapon's life cycle. Three of the most strategic questions to be answered include where special nuclear material (SNM) may have originated, what the age of the SNM may be, and how the SNM can be accurately characterized once incorporated into a nuclear device and detonated. As metallic SNM age, oxidation and irradiation produce chemical changes on the surface. Isotope ratio mass spectrometric analysis of O-isotopes in the oxide layer revealed distinct uptake of ^{18}O , representative of local water vapor values in the oxidation atmosphere. Damage from self-irradiation accumulates within both the metallic SNM and the growing oxide layer, resulting in a suppression of the outer most oxide layer, made evident through Raman spectroscopy. When these materials are fused at temperatures between 5,000 – 20,000 K in a slurry of soil, device components, and fuel material in a detonation event, hand held Laser induced breakdown spectroscopy (LIBS) coupled to partial least squares regression (PLSR) modeling resulted in accurate identification of elemental compositions (± 1 wt%). This is an invaluable standoff technique for in field analysis of nuclear debris.

TABLE OF CONTENTS

Introduction	1
Pre-Detonation Materials	3
Cu As A Surrogate For Pu	4
Aging: Cu Oxidation	6
Damage: Irradiation	8
Experimental Methodology for Material Preparation of Cu Metal	10
Electrochemical Polishing	10
Thermal Aging	11
Ion Irradiation	12
Analysis Techniques	14
Isotope Ratio Mass Spectrometry (IRMS)	14
Raman Spectroscopy	16
X-Ray Diffraction	20
Chapter 1: Time- And Temperature-Dependent Signatures of Cu Oxides through O Isotope Fractionation (LA-UR-20-23722)	22
Abstract	22
Introduction	22
Experimental Setup	25
Results	27
Raman Spectroscopy	27
Isotope Ratio Mass Spectrometry	29
Discussion	30
Conclusions And Recommendations	41
Chapter 2: Structural Modification of Cu Metal and Cu Oxide through Ion Irradiation (LA-UR-20-24516)	43
Abstract	43
Introduction	43
Experimental Setup	46
Results And Discussion	50
Conclusions And Recommendations	61
Post-Detonation Materials	62
Nuclear Underground Engineered Test Surrogates (NUGETS)	63
Environmental Standards	66
Experimental Methodology	67
NUGETS Synthesis	67
Ammonium Bifluoride Digestion	70
Analysis Techniques	70
Inductively Coupled Plasma – Optical Emission Spectroscopy (ICP-OES)	71
Handheld Laser Induced Breakdown Spectroscopy (HH-LIBS)	71
Multivariate Data Analysis: Partial Least Squares Regression (MVA: PLSR)	75

Chapter 3: Multivariate Analysis Methods Applied To Handheld Laser Induced Breakdown Spectroscopy (HHLIBS) Spectra Of Post-Detonation Synthetic Nuclear Melt Glass (LA-UR-20-25215)	78
Abstract	78
Introduction	78
Experimental Setup	81
HHLIBS Measurements	82
Point Spectra Gui Procedure	83
Results And Discussion	83
Conclusions And Recommendations	94
Conclusions	95
References	97
Vita	112

LIST OF TABLES

Table 1: Oxidation parameters for Chapters 1 and 2 aging experiments.....	13
Table 2: Input parameters for TRIM calculation and irradiation parameters.	15
Table 3: Oxygen isotope results for temperature-dependent aging experiments.....	33
Table 4: Oxygen isotope results for time-dependent aging experiments at 350°C.	33
Table 5: List of NUGET NV1X samples compositions (wt%)	65
Table 6: NIST 610 Compositional Values (wt%).....	68
Table 7: Geological Standards utilized for analytical comparison and model formation.....	69
Table 8: Sub-model ranges of the training data	84
Table 9: Weight percent concentration of elements in NUGETS and NIST610.....	86
Table 10: PLSR model formation parameters for each element.....	87
Table 11: RMSEP Values for Blended and Full Models.....	91

LIST OF FIGURES

Figure 1: Schematic of oxidation in dry air at 350 °C for Cu (left) and Pu (right).	5
Figure 2: Technical schematic of Isotope Ratio Mass Spectrometer.....	17
Figure 3: Lab Spec 6 interface for Raman measurements and processing.	19
Figure 4: Schematic illustration of beamline HPCAT 16 BM-D at the APS of Argonne National Laboratory. The monitor (1) and detector (2) ionization chambers are removed for XRD experiments using a MAR345 image plate detector [44].	21
Figure 5: Raman spectra of oxide phases on a Cu substrate exposed to accelerated aging as a function of increasing temperature each for 1 hour (left) and to accelerated aging at 350 °C as a function of increasing time (right). All measurements have been performed at room temperature and in ambient air.	28
Figure 6: Raman peak intensity of the two primary Raman modes of CuO (298 cm ⁻¹) and Cu ₂ O (220 cm ⁻¹) relative to the highest peak for each spectra. Each symbol represents one data point. The lines are included to guide the eye.	31
Figure 7: a) Isotope ratio mass spectrometry (IRMS) results of δ ¹⁸ O in Cu oxide from samples for the time-dependent series. The error bars are included (+/-4‰). b) IRMS results of temperature-dependent series for the original sample set (Run 1) with two validation sample sets (Runs 2 and 3). Sodium fluoride was added to Run 3 to improve combustion in the IRMS. The error bars are +/- 4‰ for Run 1, +/- 2.2‰ for Run 2, and +/- 0.5‰ for Run 3. Each data point represents an individually aged sample; however, lines are included to guide the eye.	32
Figure 8: Measured position of the 630 cm ⁻¹ Raman mode of CuO as a function of temperature and time.	36
Figure 9: (a-b) Variation of 1000ln(α) as a function of temperature for Cu oxides from this study compared to previously published data for other metal oxides. The fractionation factor, α, is the ratio of heavy to light oxygen isotopes in the metal oxide compared to the ratio of heavy to light isotopes in the oxygen source (atmospheric O ₂ on (a) and water vapor on (b)). Note that 1000ln(α) _{oxide-water} ≈ δ ¹⁸ O _{metal oxide} - δ ¹⁸ O _{O₂/water} . For this study, the 1000ln(α) values (in black) were calculated using the measured average δ ¹⁸ O values of Cu oxides, the known δ ¹⁸ O of +23.5 ‰ for atmospheric O ₂ [70] on (a), and the estimated δ ¹⁸ O of -17‰ for water vapor on (b) based on the δ ¹⁸ O of local precipitation of Knoxville, TN. Guide lines are included to lead the eye.	38
Figure 10: Variation of measured average δ ¹⁸ O values as a function of temperature for Cu oxides from this study (black solid and open circles) compared to the δ ¹⁸ O values of atmospheric O ₂ and water vapor (grey lines), and theoretical ranges of δ ₁₈ O estimated for Cu oxides (gray fields) using isotope fractionations with pure O ₂ gas reported by Brown [69] and Bernstein [68] and oxygen isotope exchange between various metal oxides and water reported by Zheng [71].	39
Figure 11: TRIM simulations of 10-MeV Au ³⁺ ions in Cu showing (a) the relative damage versus ion penetration depth and (b) the ion range.	48
Figure 12: Grazing incidence XRD patterns of pristine and irradiated Cu metal. The patterns are stacked for increasing level of radiation damage expressed as displacements per atom (dpa). The two diffraction maxima are indexed for the sample irradiated to 15 dpa.	52
Figure 13: (a) Raman spectrum and (b) synchrotron XRD pattern of pristine Cu oxidized at 350 °C within an ambient air furnace for 1 hour. The growth of the two Cu oxide phases (Cu ₂ O	

marked with pink dots and CuO marked with red squares) is confirmed by both techniques.
The XRD patten in (b) is indexed for both phases. 54

Figure 14: (a) Raman spectra and (b) synchrotron-based XRD patterns of irradiated Cu (10-MeV Au, 5, 10, and 15 dpa) after oxidation at 350 °C within an oxygen atmosphere. The two Cu oxide phases, Cu₂O and CuO, are marked with pink dots and red squares, respectively. 57

Figure 15: (a) Raman peak shift of CuO with respect to Cu₂O 220 peak [cm⁻¹] and (b) Raman peak intensity ratios of the 298/220 cm⁻¹ modes representative of CuO and Cu₂O, respectively. Each data point represents the peaks in labeled sample spectrum. 58

Figure 16: SEM images of pristine Cu metal (a) and Cu metal irradiated with 10 MeV Au³⁺ ions to 5 dpa (b), 10 dpa (c), and 15 dpa (d). 59

Figure 17: NV1C Sample bottom side (top left) and reflective side (top right) as compared to underground nuclear explosive melt debris (U-NEMD). 64

Figure 18: Image of Inductively Coupled Plasma-Optical Emission Spectrometer used in this study. 72

Figure 19: Example output from HHLIBS SciAps internal program. Highlighted and circled elements are indicated by image legend. 74

Figure 20: Model predictions for composition of NUGETS, NIST610, and Test Standards combined for each element plotted against actual composition values. 88

Figure 21: NUGETS and NIST610 prediction results the blended and full models for each element. 93

INTRODUCTION

The possibility of nuclear terrorism or attack is a grave global threat at present. Since the inception of the first nuclear device, Pu-239 has been at the forefront of weapon design. Major obstacles (high radioactivity, instability, and inorganic origin) impede extensive studies on the isotope due to the amalgamation of both chemical and structural effects. These transformations are exceedingly dependent on environment (atmosphere, temperature) as equally as form (reserve pits, detonated debris, etc.).

This research is largely split into the two main thrusts of nuclear forensics: pre-detonation studies and post-detonation studies. Each research focus pertains to drastically different physical systems, linked by a common chemical host – plutonium – where each chapter acts as a stand-alone section with self-contained sub-sections. Chapters 1-2 discuss characterization of plutonium primarily in its metallic form, focusing on age, thermal history, and damage accumulation. In special nuclear material (SNM), or material from which nuclear weapons are commonly designed (i.e. Pu-239), the aging of the material is affected by self-irradiation and oxidation in pre-detonation scenarios. The work presented here describes studies aimed at understanding nuclear reactions in surface environments which lead to distinctive chemical and isotopic signatures that can be harnessed for nuclear forensic purposes. Chapter 1 employs a multidisciplinary investigation of O isotopes as a geographical-dependent tracer for oxide growth, useful for identifying origin of interdicted material. The combined analysis from Raman, X-ray diffraction, and Scanning Electron Microscopy in Chapter 2 unveils how the underlying damage from alpha-decay uniquely translates to metallic oxide layer growth, indicative of material aging.

Chapter 3 details the coupling of multivariate data analysis techniques to hand-held laser induced breakdown spectroscopy for on-site quantitative analysis of nuclear debris in a post-detonation scenario. In this case, the system itself has completely transformed through massive explosion dynamics subject to high levels of radiation at temperatures between 5000-20,000 K, leaving behind melted glass debris. Successful identification of the detonated device relies in accurate characterization of the melt glass composition (Pu and its fission products, parts of the device infrastructure, as well as a host matrix comprised of the surrounding soil). Through combination of Chapters 1-3, a selection of shortcomings in accurate characterization of the Pu-system are highlighted and improved upon.

PRE-DETONATION MATERIALS

There is a critical need in nuclear forensics for a novel technique able to rapidly and effectively characterize intercepted special nuclear material (SNM). Some SNM exists in alloyed systems, such as PuGa, and present distinct signatures as they undergo aging [1-3]. The signatures that emerge include changes in electrical transport properties, structural defects due to self-irradiation, and surface oxide formation and growth. These alloys are also subject to elevated temperatures during fabrication, operation, and the decay heat of Pu-239 [4,5]. Thus, high temperatures must be an integral part of aging studies as well as an understanding of damage accumulation from self-irradiation. δ -phase Pu is desirable due to its tough and malleable properties, but only possible when pure Pu is kept at high temperatures [6]. To keep the δ -phase at room-temperature it must be alloyed with ~3wt% Ga (or another element such as Al) for it to resist transforming back to its stable alpha phase. The introduction of the new alloying element can complicate damage accumulation in the bulk material [7]. A technique to determine the age of the material which is developed off the changing surface of SNM would therefore be valuable. The leading analysis techniques for pre-detonation material include a variety of radiochronometry methods. Utilizing actinide ratios such as $^{235}\text{U}/^{239}\text{Pu}$, etc. depending on target material provides information into compositional history of the radioactive elements [8]. These studies are often validated on Standard Reference Material (SRM). The most popular methods fall into either decay counting such as gamma or alpha spectrometry or mass counting methods such as Secondary Ion Mass Spectrometry (SIMS), Thermal Ionization Mass Spectrometry (TIMS), or Inductively Coupled Plasma – Mass Spectrometry (ICP-MS) [9]. However, the decay counting techniques require larger sample masses and the mass counting techniques are largely destructive – both of which are minimized in the following Chapters. The experiments in Chapters 1 and 2 test new forensic

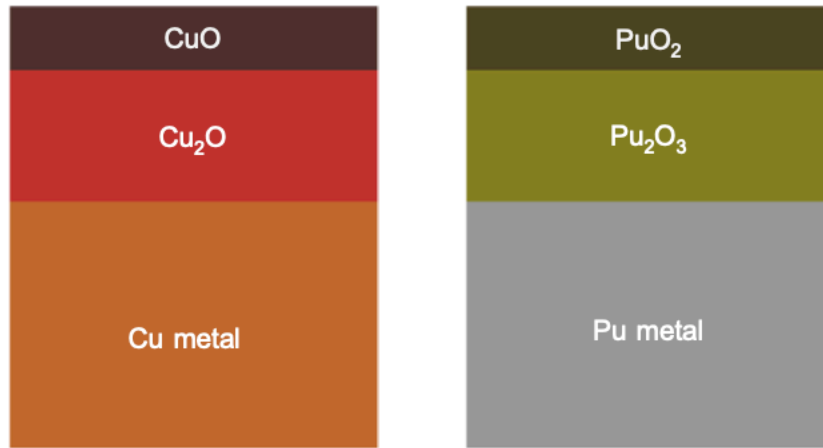
signatures that focus on the oxidation of SNM utilizing Cu as an analogue material through: (i) a reference case (without radiation damage) and (ii) a more realistic case (with radiation damage).

Cu as a surrogate for Pu

Changes in chemistry of Cu such as surface oxidation [4, 10-11] as well as radiation damage [12-15] are extremely well understood making comparisons to literature significantly more accessible. Pu and Cu metal share a common crystal structure (face centered cubic, FCC). They also undergo similar oxidation growth (Fig. 1). The increasing damage inflicted in Cu metal by ion irradiation and subsequent oxidation formation mimics the oxidation of Pu systems. In elevated temperatures (350 °C) and dry environments, a thicker initial layer of lower valence state Pu³⁺ (Pu₂O₃) and then a thinner higher valence state Pu⁴⁺ (PuO₂) forms on top as measured by XRD and XPS in a study by Haschke, *et al.* [5]

The sequence of these oxide species remain markedly similar to Cu (Cu₂O followed by CuO at temperatures above 320 °C). The layering of oxide layers observed at 350 °C indicates a change in mechanism observed through a break in the parabolic oxidation curve which is known to be caused by two different protective oxides in the Cu system [4]. Furthermore, at a temperature of 350 °C with increasing damage inflicted on a grown Cu oxide (bulk), a lesser fraction of CuO is observed than without damage at the same temperature much like with Pu oxide (bulk) at elevated temperatures and increasing time scales (correlated to damage), there appears to be a lesser amount of PuO₂ [4]. This is due to the further reduction of PuO₂ into Pu₂O₃.

Stakebake validated that the lesser oxides of Pu form above 350°C, and that the increase in oxidation time in the PuGa systems causes a similar trend in O gain as seen in the Cu oxide system [4]. In summary, as δ phase Pu and Cu oxidize, they undergo similar O adsorption, oxide phase growth, and growth mechanisms with increasing temperature and time, in similar environments.



*approximate layer ratios, not draw to scale

Figure 1: Schematic of oxidation in dry air at 350 °C for Cu (left) and Pu (right).

Therefore, if the same characterization methods are applied to Pu oxide surface as proposed on irradiated Cu oxide surfaces, we should be able to draw a convincing comparison.

Aging: Cu Oxidation

Accelerated aging at elevated temperatures is one of the methods commonly used to simulate natural aging in materials beyond laboratory time frames. The theory is that the basic reaction rate equation includes dependencies for time and temperature, and thus, is able to be manipulated to produce the results often seen in long time-scales in shorter periods by increasing the temperature. Sometimes it is used in a cyclical process until the desired effects are produced. This process is routinely applied to a variety of materials including both metals and polymers [16-19]. Wright completed a study on Inconel 617, a Ni-Cr-Co-Mo alloy, where thermal aging is applied to examine oxide grain growth with increasing time and temperature as well as the alloy's performance under stress loading [17]. Wang observed thermal aging effects on thin films of tin upon a Cu substrate where the oxide growth was measured as thickening in air, and the species of oxides that formed was dependent on temperature [18,19]. These types of experiments are plentiful, providing a rich background on the thermal aging and oxidation of metals and are aligned to what is proposed in the sections below. It is the goal of these aging experiments to explore both time- and temperature-dependent effects, as well as those induced by irradiation at a fixed time and temperature.

Oxide formation on Cu(110) metal is offered to aid in the conceptualizing the growth processes [4]. Oxidation is initiated when a thin layer of O is chemisorbed on the metal surface, producing a monolayer string of Cu-O-Cu-O [10,11]. The presence of excess O molecules creates cation vacancies at the surface of the oxide-air interface by bonding with two electrons from the Cu. This effect creates a concentration gradient of copper vacancies through which copper ions are then

able to move, forced by the electric field between the Cu and chemisorbed O. The phenomenon is outlined by the Wagner model which attributes oxidation to the diffusion of ions in a system that is electrically conductive driven by the decreasing concentration of copper vacancies from the surface (air) to the metal (copper) [10,11]. Additionally, during the initial formation of Cu₂O, the O vacancies are present in the structure, providing an avenue for O ion diffusion to the Cu surface to a lesser degree [20].

The fractionation of O isotopes into the Cu oxide is determined by oxidants present, bonding environment in the formation of the oxide layer, and temperature. There are three well-studied Cu oxide phases. The Cu¹⁺ ion is 2-fold coordinated with O²⁻ ion for Cu₂O in a cubic structure (space group *Pn-3m*) and the Cu²⁺ ion is 4-fold coordinated with O²⁻ for CuO in a monoclinic structure (space group *C 2/c*). The Cu₄O₃ phase is a tetragonal mixed valence metastable phase, which can be visualized as a cubic crystal structure with a monoclinic distortion (space group *I41/amd*) [21,22]. As O dissociates on the surface of Cu metal (FCC crystal structure), they fall into the tetrahedral interstitial sites and the Cu metal reconstructs around the O atoms forming Cu₂O islands [23].

These islands grow to a point of saturation, where they coalesce. In this temperature range (250 °C – 400 °C), the predominant mechanism for continued oxide growth for both phases is through grain boundary diffusion among the Cu₂O layer. The size of Cu₂O grains do not grow to the point of allowing lattice diffusion until approximately 600 °C [24]. Oxidation is rate limited by the diffusion through this oxide layer, which is influenced by temperature [25]. Because isotopic fractionations of light elements such as oxygen are usually temperature-dependent, the ability to correlate oxygen isotope composition to temperature would provide an invaluable forensic tool as Pu metal ages.

Damage: Irradiation

Effects from aging of Pu are not only observed in chemical processes, but through radioactive decay. When Pu decays, it does so by splitting into a U atom and an α particle. While the α particle predominantly creates helium bubbles, the recoil energy off the U atom is dissipated by displacements of Pu atoms from their original lattice sites, leaving vacancies beyond and forming interstitials which, depending on the temperature, become mobile and form clusters [5]. The creation of both He bubbles and voids cause overall swelling in the lattice. This is the result for almost every metallic compound subject to high levels of radiation at a fraction of 1/3 its melting temperature [5, 26-27]. In order to simulate SNM evolution over a life-time of radiation exposure, ion irradiation is often employed. This induces damage effects correlating to alpha-decay damage, critical to our understanding of defect accumulation in SNM. In many studies, surrogates are used as detailed above to test techniques for a cheaper cost - specifically those in the FCC family when the SNM of interest is PuGa alloys. Each ion creates a collision cascade where a high concentration of point defects is produced within a nm-sized zone. The majority of these defects spontaneously recombine during the quenching of the cascade, but a small fraction agglomerate and form defect clusters. Defects that are outside of the spontaneous recombination radius may become freely migrating vacancies or interstitials [27]. Understanding how these defects form and mobilize allows one to predict material property transformations.

The variety of defects induced through irradiation often make it difficult to quantify damage specifically. Often displacements per atom (dpa) is employed as a way to compare across differing types of irradiation studies (ion, neutron, electron, etc.) and defects produced. The damage can be approximated using James Ziegler's program SRIM (Stopping and Range of Ions in Matter) [28]. SRIM is a collection of software packages that calculate many features of the transport of ions in

matter. It uses Monte Carlo techniques to model ion beam interactions in targets. It calculates damage energies, full cascades, and has graphics representations of ion paths so one can get qualitative information about where the most ion damage is occurring. This specific part of the program is called TRIM (**T**ransport of **I**ons in **M**atter). These codes allow one to enter in a variety of experimental parameters and calculate results including but not limited to penetration depth and ion energy loss (based on target material stopping powers). By choosing parameters corresponding to Pu self-irradiation defect accumulation rate of 0.1 dpa per year, similar damage can be induced in other FCC metals such as Cu through heavy ion irradiation [27]. Ion irradiation can be used to achieve high displacement rates in a short duration of time. This means, to simulate for damage accumulated in Pu in 50, 100, and 150 years, there needs to be 5, 10, and 15 dpa worth of damage inducted in the Cu. The TRIM code cannot directly calculate dpa, but there is a method described by Stoller *et al.* that allows for an accurate damage calculation using TRIM utilizing the “quick” Kinchin-Pease model to compute the damage. Stoller et al. found this method to give a better approximation for the damage than the standard TRIM calculation [28]. The method includes setting the lattice and binding energies to zero. The Kinchin-Pease model gives the number of Frenkel pairs produced per ion as:

Eq. 1
$$v = 0.8T_{dam}(E_{PKA})/2E_d$$

The average damage per ion (dpi) per length is then given by v/l , where l is the effective range of the ions. T_{dam} is the damage energy of each recoil, E_{PKA} is the energy of the primary knock-on atom, and E_d is the threshold displacement energy. The required fluence Φ to reach the targeted dpa levels was calculated based on:

Eq. 2
$$\Phi = \frac{dpa}{dpi} \Omega$$

where Ω is the atomic density. Finally, the time for irradiation may be obtained from:

Eq. 3
$$t = \frac{\Phi}{\Omega}$$

where Φ is the flux of the beam.

Experimental Methodology for Material Preparation of Cu metal

The Cu metal used in Chapter 1 and 2 were 99.9% pure and were cut to specified (in each respective Chapter) sized squares of 0.8 mm thick sheet of Cu metal purchased from McMaster-Carr ®. The samples were all stored in a nitrogen glove box between electrochemical polishing, oxidation, ion irradiation, and all following analysis techniques. A set of complementary techniques were utilized for pre-detonation research (Chapters 1 and 2) as outlined below.

Electrochemical Polishing

Electrochemical polishing is used in many industries as a way to gently clean the surface of metals [29]. A clean, reproducible surface was key to the aging experiments requiring a careful and reproducible polishing procedure. By applying a current through a metal within a solution medium, the outermost layer of the Cu squares is removed through a process similar to reverse hydrolysis. In this research, the solution is a mixture of deionized water (DI) with 2 wt% KOH. A pair of stainless-steel curved tweezers are placed into the solution on the lip of the beaker to serve as the anode (AT). Another set of tweezers are then tapped to a non-conducting rod and used as the cathode (CT). The voltage source (Lavolta BPS305 Variable Linear DC Power Supply) is set

parallel to the magnetic stirring plate, and the negative and positive alligator clips is attached to the base of the anode and cathode tweezers, respectively. A small beaker of pure deionized water is placed within the fume hood as well as for sample rinsing between polishing segments. The first sample is pinched by the CT and held in place by clamping the alligator clip mid-way down the tweezers. It is crucial to ensure that the tweezers did not cover a substantial portion of the Cu square surface area, therefore, a priority should be to pinch as close to the sample edge as possible. Holding the CT at the non-conducting end, the following steps are taken [30]:

1. A 17.5 V source is applied to the stirred solution while the Cu square is submerged completely and parallel to the current flow of the liquid.
2. The sample is left for 20 seconds, taken out of solution and dipped into DI for quick rinse.
3. The voltage is increased to 25 V and step 2 is repeated.
4. The voltage is increased to 30 V and allowed to dry on a clean surface.
5. Steps 1-4 are repeated until all samples were polished; the 2 wt% KOH solution should be changed after every 4-5 samples to avoid deposition of impurities gathered from the solution back onto the sample surface.

Thermal Aging

Once the polished Cu samples are dry, they are placed atop an Al₂O₃ (alumina) circular disc and inserted into the furnace for heating. Alumina was chosen as an inert high-temperature tolerant ceramic to minimize the possibility of either reaction or O diffusion from the substrate to the Cu matrix. The ramp-up rate is set 10 °C per minute with a dwell time varying for the appropriate experiment as shown in Table 1. There was no ramp-down rate set and the furnace was allowed to cool while switched off until the inside temperature reached below 100 °C. It is important to note that each sample is to be run individually and that no interruption in heating regime occurs. The

samples were then removed with metal tongs and allowed to further cool to room temperature before being further analyzed. The inner atmosphere of the furnace itself was not controlled to any set humidity in order to simulate realistic conditions of natural oxidation occurring during exposure to air. Chapter 1 experiments were performed in 3 independent runs:

- (i) one set of polished, oxidized Cu square samples for both temperature- and time-dependent experiments.
- (ii) and (iii) two separate sets of Cu square samples for validation of IRMS measurements of the temperature-dependent experiments.

All three runs were used for the temperature-dependent series to assess data reproducibility of O isotope fractionation in the Cu oxide phases. Also, NaF was added to Run 3 in order to assess whether the reagent had an effect on Cu oxide combustion which ensures that the whole sample was analyzed for $\delta^{18}\text{O}$. Chapter 2 experiments were performed as one run with all experimental parameters remaining the same except for a fixed dwell time of one hour at 350°C for all samples (Table 1).

Ion Irradiation

As previously mentioned, the decay of Pu in PuGa alloys over time creates radiation damage, which affects a materials structure and thus provides a traceable change in the oxidation process [1-4, 26]. It is the goal of this study to mimic this environment through ion irradiation in a surrogate metal. Three 6×6 mm Cu squares that are 0.8 mm thick are to be irradiated with 10 MeV Au³⁺ ions at a particle flux of 1×10^{12} ions/cm²/s. The irradiations were performed at the Ion Beam Materials (IBML) accelerator at the University of Tennessee. For the calculations in SRIM, 10 MeV Au³⁺ ions at the aforementioned flux of 10^{12} ions/cm²/sec is input with the target as pure Cu metal at a density of 8.92 g/cm³ to produce estimated damage shown in Table 2 below.

Table 1: Oxidation parameters for Chapters 1 and 2 aging experiments.

	Temperature	Time
Temperature-dependent Series (Ch. 1)	250 °C	1 hour
	300 °C	1 hour
	350 °C	1 hour
	400 °C	1 hour
Time-dependent Series (Ch. 1)	350 °C	1.5 hours
	350 °C	2 hours
	350 °C	2.5 hours
	350 °C	3 hours
	350 °C	3.5 hours
Irradiation Series (Ch. 2)	350°C	1 hour

Correlating to the 0.1 dpa/year naturally produced in Pu through self-irradiation, it is the aim of this study to track 50, 100, and 150 years of damage (5, 10, and 15 dpa respectively). This wide time span was selected in order to enhance the effects that may occur. A MATLAB code was created that takes the SRIM output together with the beam input parameters and gives an irradiation time (Eq. 1-3). The dpa value calculated using [28] is to be interpreted as an average dpa over the total irradiated range, which one can see in Figure 5. For this reason, we used Au ions, which have a flatter damage profile when compared to lighter ions such as Ni. Each sample was prepared individually so as to not expose it to the heat for any longer than necessary. The irradiation is estimated to take a total of 14 hours with the beam setup and stabilization. The samples were irradiated at a temperature of 200 °C corresponding to approximately $0.35T_M$ of Cu. The difference in defect recovery at room temperature vs. 200 °C is significant but is at this temperature that microstructure evolution is most readily observed [31]. From our preliminary calculations, we are estimated a beam current of 250 nA.

Analysis Techniques

Isotope Ratio Mass Spectrometry (IRMS)

Materials experience isotopic fractionation, or the active separation of isotopes of a single element, due to chemical, physical, and biological influences with two major influences being temperature and pressure. This creates distinct signatures which are able to discern origin, history, age, etc. of a given material. Isotope Ratio Mass Spectrometers (Fig. 2) have been popular for use in origin studies in geochemistry, archaeology, and forensic studies due to their ability to precisely and accurately measure natural stable isotopic abundance of light elements (H, C, N, O, S) [33,34]. Specifically, in explosives, IRMS has proved to be a useful tool for differentiating among isotopes of ammonium nitrate and certain plastics in trace amounts [35,36].

Table 2: Input parameters for TRIM calculation and irradiation parameters.

List of irradiation conditions			
Sample	A	B	C
Ion beam	Au ³⁺	Au ³⁺	Au ³⁺
Total dose (dpa)	5	10	15
Fluence (ions/cm ² /s)	1.63 x 10 ¹⁵	3.26 x 10 ¹⁵	4.89 x 10 ¹⁵
Time (min)	27	54	82
Temperature (°C)	200	200	200
Input parameters for TRIM calculations		Relevant Output parameters from TRIM calculations	
Ion species	Au ³⁺	Ion energy loss	0.08%
Ion energy (MeV)	10	Atom energy loss	32.62%
Target width (mm)	0.8	*losses due to phonons	
Target density (g/cm ³)	8.92		
Target composition	Cu		
Displacement energy [32] (eV)	30		
Surface and binding energies (eV)	0		
Number of ions	100,000		

In the field of nuclear studies, IRMS has recently been used for the preparation and validation of Pu age dating materials [8]. Namely, for evidence towards material accountancy declarations, as well as origin of material. There are several mechanisms contributing to the effectiveness of this technique in such high-stake studies. The rapid results inherent in most spectroscopic and spectrometric techniques is one of the most attractive qualities of IRMS.

Initially, the sample is injected into the inlet of the spectrometer where it is vaporized and transferred to a column with use of helium as a carrier gas. It is then allowed to react with both the carrier gas and inner coating of the column to separate the compounds desired for measurement, sweeping the resultant mixture into a combustion chamber where they are oxidatively combusted into a simple gas, such as CO, CO₂, H₂, or N₂. Any water is removed from the system by passing this stream of gas through a selectively permeable tube and then sending it through a basic electron ionization device to create ions [37].

The gas ions are further guided along the spectrometer by a bending magnet (magnetic sector analyzer), separating the ions based on mass through this process, and collides the separated stream of ions with a series of faraday cups, lined up to match each mass of isotope. IRMS measures the continuous flow of these ions (Fig. 2). By measuring the O isotope fractionation in Cu oxide layer grown of the pristine thermal aging experiments at each time and temperature, this technique allows insight to the probable relationship between fractionation and specific oxide species formation.

Raman Spectroscopy

In Raman measurements, a beam of monochromatic light is directed at the sample surface, and its electromagnetic field interacts with the electrons of the sample, causing a change in polarizability.

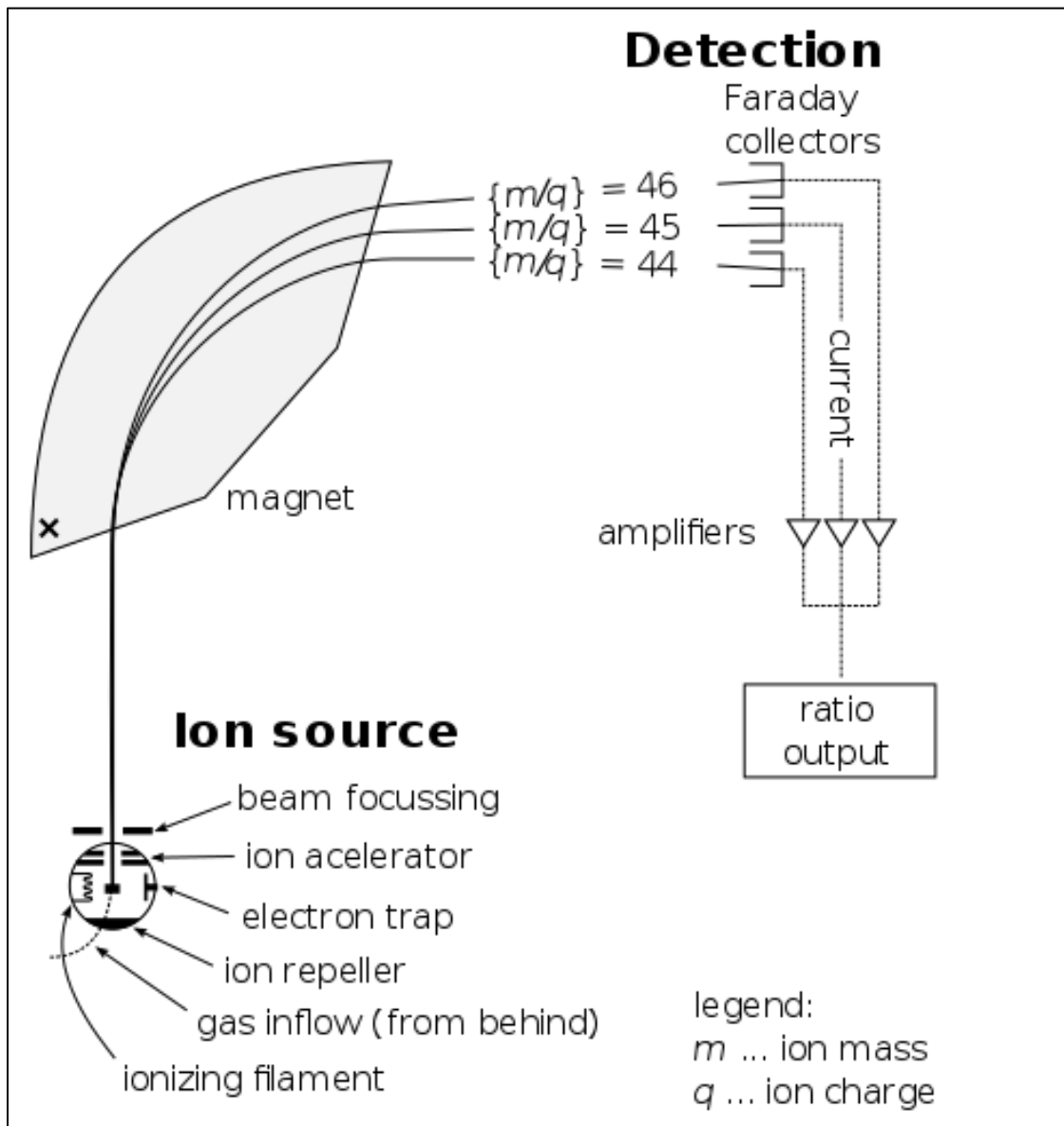


Figure 2: Technical schematic of Isotope Ratio Mass Spectrometer.

These electrons typically elastically scatter the light (Rayleigh scattering), but a fraction of electrons is shifted (Stokes and Anti-Stokes scattering). The change of wavelength in the emitted light is characteristic of a specific vibrational state and can be used to identify different material phases. The light directed on the sample causes a temporary deformation in the molecular structure through electromagnetic interference and induced vibrations at a characteristic frequency. The pathway that the molecule or bonding environment scatters the excess energy depends on its initial state. The elastic scattering is unideal for Raman measurements, and oftentimes is blocked by the use of special apertures so that the weaker signals from inelastic scattering can be more clearly recorded [38].

This is because elastic scattering represents a net loss in energy, where the energy imparted onto the sample is exactly reflected, thus we cannot gain any useful energetic information from the measurement. Raman spectroscopy can provide insight into local bonding structure as well as fraction of crystal species in the sample derived from peak analysis. In current studies of nuclear forensics, Raman has been used to characterize uranium tetrafluoride (UF_4) [39], seized uranium-containing material [40], and zirconium-uranium alloys from the Chernobyl nuclear power plant [41]. Relevant to the study in this dissertation, it is widely utilized in UO_2 studies [42], and temperature dependence of its oxide formation [43].

A Micro-Raman Horiba LabRAM HR Evolution spectrometer was be utilized in this research to acquire spectra of all time-, temperature-, and irradiation-dependent series of oxidized Cu samples. The Raman is confocal, so the information obtained from these measurements are representative of the near-surface regions. Previous to any measurement, the spectrometer was calibrated with a Si standard. The software package Lab Spec 6, was employed to control all parameters, focus the lens, and display the collected spectra (Fig. 3).

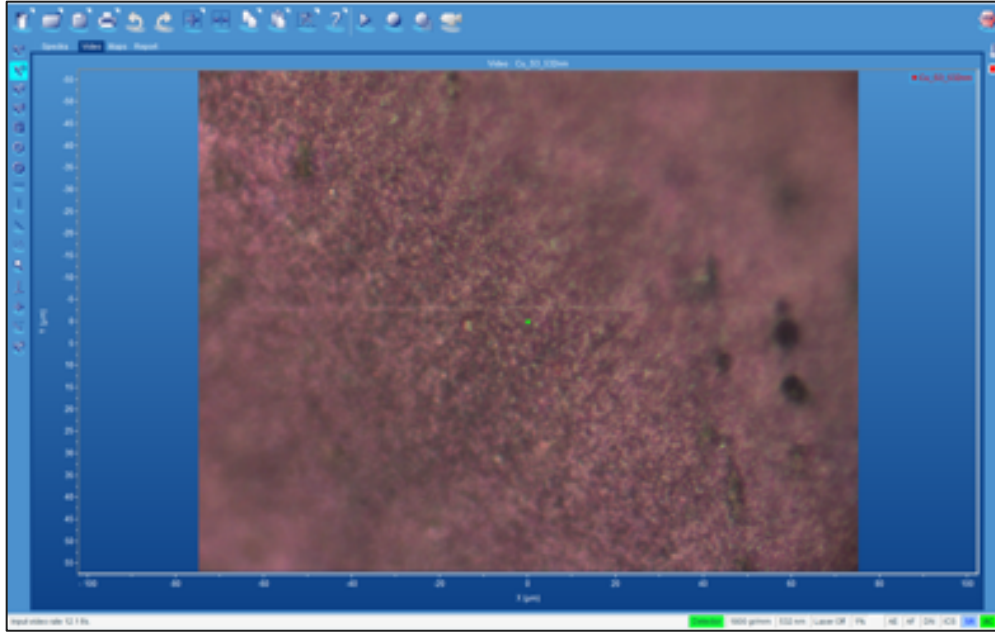


Figure 3: Lab Spec 6 interface for Raman measurements and processing.

X-ray Diffraction

Grazing incident X-ray Diffraction (GIXRD) was utilized in this research to gain structural information on the surface of irradiated Cu metal in order to capture the thin layer of damage induced through ion irradiation. A Panalytical X'Pert3 MRD was utilized in grazing-incidence mode due to the shallow depth of the ion-beam damage. The measurements were conducted using the Cu K- α wavelength of 1.54 Å with a fixed divergence slit of 0.05 mm and continuous scan range of 5° to 70° on all four samples. The incident grazing angle was 1°, which corresponds to a measurement depth of approximately 0.9 μm , considering a Cu density of 8.94 g/cm³ and a packing factor of ~ 1 . GIXRD was performed at the Joint Institute for Advanced Materials (JIAM) Diffraction Facility, located at the University of Tennessee, Knoxville.

Additional XRD measurements were conducted using only small amounts of powder through synchrotron X-rays. Adopted from the small sample volumes that are characteristic of high-pressure experimental procedures, microscopic sample chambers are prepared in a thin molybdenum foil by drilling several holes with a diameter of $\sim 100 \mu\text{m}$. The foil thickness was 50 μm . Sample chambers are cleaned in an ultrasonic bath with acetone, and the sample powder is placed over the holes and pressed between two steel die-pieces in a hydraulic laboratory press. Synchrotron X-ray analysis are performed at the Advanced Photon Source (APS) of Argonne National Laboratory using sector 16 (HPCAT, High-Pressure *Collaborative Access Team*) (Fig. 4) [44]. A highly-focused X-ray beam (spot size 25 μm) is used to study structural properties of the Cu oxide sample in transmission mode by means of angle-dispersive micro X-ray diffraction (XRD).

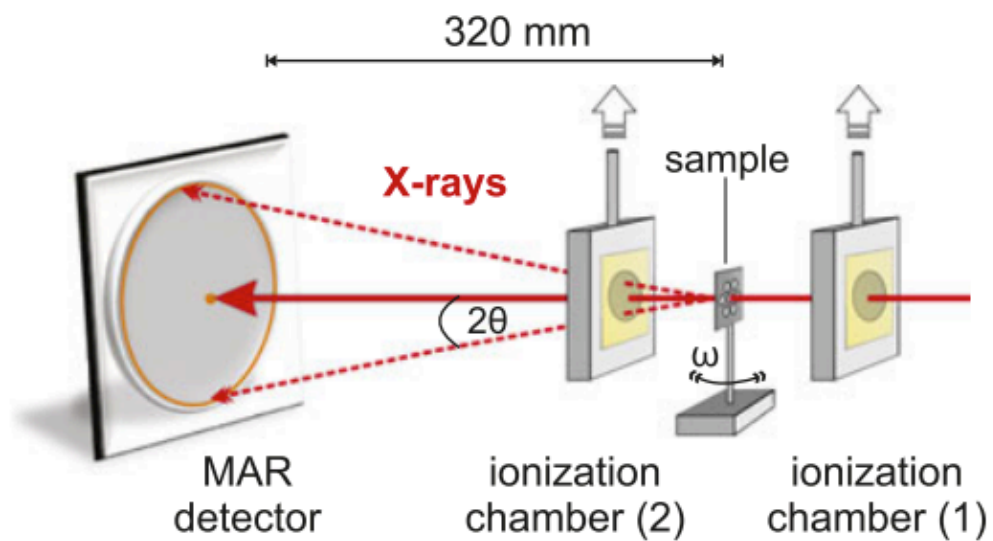


Figure 4: Schematic illustration of beamline HPCAT 16 BM-D at the APS of Argonne National Laboratory. The monitor (1) and detector (2) ionization chambers are removed for XRD experiments using a MAR345 image plate detector [44].

CHAPTER 1: TIME- AND TEMPERATURE-DEPENDENT SIGNATURES OF CU OXIDES THROUGH O ISOTOPE FRACTIONATION (LA-UR-20-23722)

Abstract

In an effort to provide a time- and temperature-dependent signatures reliable for characterizing special nuclear material (SNM), copper metal was utilized as a surrogate for metallic actinide materials and subject to accelerated aging through thermal treatment. A multiphase oxide-layer growth of Cu_2O and CuO was detected which depended on temperature (250 – 400 °C) and aging time (1 – 3.5 hours). Isotope ratio mass spectrometry and Raman spectroscopy were used as complementary analytical approaches to investigate the mechanism of copper oxide formation. A linearly correlated temperature-dependent isotopic fractionation of oxygen was found, exhibiting negative $\delta^{18}\text{O}$ values that are equivalent to an increasing enrichment of copper oxides in light ^{16}O isotopes with increasing temperature. The distinctive negative $\delta^{18}\text{O}$ values are associated with the isotopic fractionation between main oxidant (atmospheric oxygen) and Cu oxide phases, and subsequent oxygen isotope exchange with water vapor. Raman spectra provided further insight into the phase fractions of Cu_2O and CuO and local bonding environment of these two oxide phases with increasing temperature. The results from this study show that the oxygen isotopes ($\delta^{18}\text{O}$) are a useful tracer for studying oxide layer growth from aging of metallic systems; thus, this feature might be a key signature for applications in nuclear forensics.

Introduction

There is a critical need in nuclear forensics for a novel technique able to rapidly and effectively characterize intercepted special nuclear material (SNM) [45]. Pu metal, a component of SNM, is routinely exposed to high temperature (>200 °C) in a variety of manufacturing processes triggering oxidation as well as constant radiation damage from internal alpha decay from Pu-239 generating

defects in the crystal structure [46]. The complex transformation of these materials often complicates the ability to chemically characterize them. Typically, forms of radiochronometry are employed to ratio products of the naturally decaying Pu-239.

However, these types of analysis are destructive – requiring complete digestion of the material for measurement using a mass spectrometer, most commonly Secondary Ion Mass Spectrometry (SIMS), Thermal Ionization Mass Spectrometry (TIMS), and Inductively Coupled Plasma Mass Spectrometry (ICP-MS). Routine inspections of nuclear facilities and inventory of stockpile materials subjects the investigative party to a variety of Pu-containing materials. It is imperative that the analysis of these materials is quick to minimize exposure, while maintaining as much of the integrity of the sample and accuracy of analysis as possible. Because safety is an essential component to the motivation behind this research, in testing new techniques, Cu metal is used as a surrogate to δ -phase Pu metal and its alloys. Cu not only shares a crystal structure to δ -phase Pu (face centered cubic (FCC)) but also undergoes similar oxidation formation mechanisms at similar temperature and environments [47]. Utilizing the Cu oxide layer growth as a forensic signature minimizes some risks associated with handling SNM as well as maintain the cohesion of the core sample.

Oxide formation and layering of oxide species during thermal treatment has been studied *ad nauseum*, but often overlooked is the fractionation of stable oxygen (O) isotopes inherent to these processes [48-50]. Isotopic fractionation refers to the separation of the variable masses of each element, dependent on the number of neutrons in the nucleus. Isotopic fractionation may occur in systems undergoing phase changes such as condensation, evaporation, and precipitation or during chemical reactions such as oxidation which affect the relative abundance of each isotope in the system. For example, lighter O isotopes (^{16}O) are incorporated into water vapor during

evaporation, making the residual water enriched in heavier O isotopes (^{18}O). Because oxidation is a kinetic process, a preferential uptake of lighter O isotopes is expected in the product. The O isotope composition in a sample is expressed using the following equation [51]:

$$\delta^{18}\text{O} = \frac{\frac{^{18}\text{O}}{^{16}\text{O}}_{\text{sample}} - \frac{^{18}\text{O}}{^{16}\text{O}}_{\text{standard}}}{\frac{^{18}\text{O}}{^{16}\text{O}}_{\text{standard}}} * 1000 \text{ [‰]}$$

where the ratio of $^{18}\text{O}/^{16}\text{O}$ isotopes in the sample is determined using isotope ratio mass spectrometry (IRMS) and compared to the same O isotope ratio of an international standard with known isotope composition. This method is used in geological applications to derive information on climate, temperature history, and mineral formation, which are usually controlled by kinetic and/or equilibrium isotope fractionations taking place in the surrounding environment [52]. More applicable to materials research is the use of O isotopes in corrosion sciences as tracers for temperature effects on various metallic pipes and components [53-56]. This study aims to investigate the oxidation growth and simultaneous O isotope fractionation on the surface of Cu metal with air under time- and temperature-dependent thermal aging experiment.

To further support the IRMS measurements of this study, Raman spectroscopy was employed for each aging experiment to gain insight into the local bonding environment and phase fractions of the different oxides. The literature on O isotope behavior in different metal oxide phases is not well established at temperatures between 250 °C and 400 °C. It has been proposed that the effect of isotope exchange can be neglected apart from a change in mass, and consequential shift in Raman vibrational mode as caused by a distortion in crystal lattice [56].

However, in the past two decades studies have shown that isotopic fractionation can cause changes in other properties such as thermal conductivity and elasticity, making it critical to understand the underlying mechanisms [57]. Motivated by commitment to global security, the implications of this study are two-fold: (i) to improve accurate identification of aged SNM alloys and (ii) to highlight the importance of isotopic fractionations in an accelerated oxide growth.

Experimental Setup

A total of nine McMaster-Carr® copper (Cu) samples were analyzed which were prepared as 6 x 6 mm² square plates cut from a 99.9% pure 0.8 mm thick Cu metal sheet. In a first experiment, four Cu squares were heated for 1 hour at 250 °C, 300 °C, 350 °C, and 400 °C, and in a second experiment five Cu squares were heated at 350 °C for 1.5, 2, 2.5, 3, and 3.5 hours. The sheet of Cu was initially protected by a plastic coating to prevent oxidation, which left a residue on the surface of the material upon removal.

To create an impurity free base layer for oxidation experiments, all Cu squares were polished electrochemically at the beginning of each experiment, previous to heat treatment, in a solution of 2 wt.% potassium hydroxide (KOH) at room temperature following the procedure in [30]. After drying in ambient air, they were placed in a Carbolite High Temperature Furnace 1800 and heat treated for their respective times and temperatures in an ambient air environment. The laboratory is temperature controlled at approximately 20 °C year-round with no humidity control.

A Micro-Raman Horiba LabRAM HR Evolution spectrometer was utilized in this study to acquire spectra of all time- and temperature-dependent series of oxidized copper samples. A spectral range from 100 cm⁻¹ to 1200 cm⁻¹ was used with a green laser of 532 nm as excitation source. The spectra were recorded with a liquid nitrogen-cooled charge coupled device detector. Previous to any

measurement, the machine was calibrated with a Si sample to ensure all components were functioning and would produce reliable spectra.

A 50x magnification objective was used to focus on the oxide layer surface in atmospheric air with a laser power of 1%. This low power was selected to avoid heating and potentially further oxidizing the samples. The Raman spectrometer was operated in confocal mode with a beam-spot size of ~ 2 μm . All spectra were recorded by two accumulations of 60 second measurements for each sample. The software package Lab Spec 6, was employed to control all parameters, focus the lens, and display the collected spectra. Both the time- and temperature-dependent series Cu oxide samples were measured with Raman spectroscopy.

After thermal treatment and Raman spectroscopy characterization, the oxidation layer produced on the surface of each Cu sample was scraped off using a stainless-steel laboratory scalpel onto a solid aluminum polished plate. The scraped powder was then filled into a small silver foil capsule until the sample mass was between 0.25 and 0.50 mg. The capsule was folded into a sphere, then placed into a sample holder and allowed to set for 2 hours at 60 °C in air to ensure samples had been removed of all moisture before being dropped into the elemental analyzer (EA) for final combustion.

The Cu oxide samples were decomposed into a CO gas in the EA utilizing helium gas as a purge for the system and analyzed for O isotope composition ($\delta^{18}\text{O}$) using a Delta Plus XL mass spectrometer. The O isotope results are reported in units of per mil with respect to the Vienna Standard Mean Ocean Water (V-SMOW). Standard deviation of $\delta^{18}\text{O}$ analysis varied between individual runs, from ± 0.5 ‰ to ± 4.0 ‰. Since the oxide layer was scraped off, the measured $\delta^{18}\text{O}$ presented in this paper represents a bulk composition of the entire thickness and different oxide phases formed at different temperatures.

Results

Raman Spectroscopy

Raman spectroscopy was used to gain insight into vibrational signatures of different oxide phases which form on the Cu surface as a function of annealing temperature and time. Several Raman modes are observable that change as a function of temperature and time (Fig. 2). Raman peaks at 297 cm^{-1} , 345 cm^{-1} , 630 cm^{-1} , and 1130 cm^{-1} are attributed to CuO [58,59], while peaks at 148 cm^{-1} , 220 cm^{-1} , and 417 cm^{-1} are associated with Cu₂O [58-60]. The Raman peak at 510 cm^{-1} represents Cu₄O₃, an intermediate oxide phase comprised of both Cu²⁺ and Cu¹⁺ ions [61].

Both Cu oxide phases are evident in Raman spectra over the entire temperature range and heating times. However, the temperature-dependent series contain predominantly Cu₂O on the sample surface at lower temperatures and a mix of Cu₂O, Cu₄O₃, and CuO, at higher temperatures, which is in agreement with previous accelerated oxidation studies at elevated temperatures [62]. The time-dependent series maintains the mixture of all Cu oxides, with a larger presence of CuO appearing only after 3.5 hours. Raman spectroscopy is a surface technique and not tuned to measure oxide thickness, however from peak intensity analysis, it is possible to gain some insight to relative oxide growth.

The total thickness of oxide layer is a function of oxidation time, but the depth is also influenced by temperature, i.e. the oxide layer still grows in both cases, but the time-dependent series is characterized by a deep growth in the oxide layer while retaining a similar surface composition and the temperature-dependent series is characterized by the formation of new surface phases [63]. With increasing time, a consistently high Cu₂O peak is visible until after 3.5 hours, when the peak height of CuO becomes dominant, indicating that a certain level of CuO thickness has developed to measure more intensely than the subsurface Cu₂O layer.

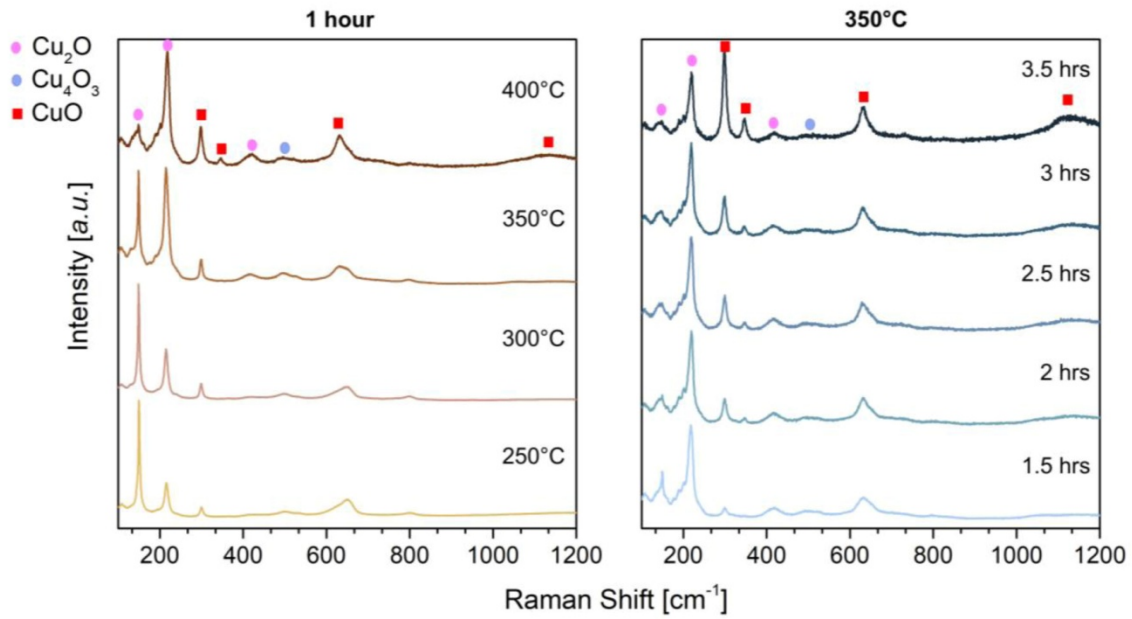


Figure 5: Raman spectra of oxide phases on a Cu substrate exposed to accelerated aging as a function of increasing temperature each for 1 hour (left) and to accelerated aging at 350 °C as a function of increasing time (right). All measurements have been performed at room temperature and in ambient air.

With increasing temperature, the peak intensities for Cu₂O and CuO in the temperature-dependent series begin at lower intensities than the time-dependent series and the trend for CuO is positively linear. This is representative of an incomplete formation of the Cu₂O layer until 350°C. This distinction in growth and oxide surface abundance between series is confirmed by literature and expressed in the series' relative peak shifts (Fig. 6) [63,64].

Isotope Ratio Mass Spectrometry

The $\delta^{18}\text{O}$ of temperature-dependent series differed significantly from the time-dependent series. The temperature-dependent experiment showed a continuous enrichment in ¹⁶O isotopes (e.g., decreasing $\delta^{18}\text{O}$ value) in the oxide layer with increasing temperature, characterized by a distinctive linear trend (Fig. 7b, Table 3) from -7.8 to -28.6‰. In contrast to the temperature-dependent aging experiment, the measured $\delta^{18}\text{O}$ varied from -30.3 to -21.3‰ with no distinct trend for samples oxidized at 350°C between 1.5 to 3.5 hours (Fig. 7a, Table 4). The key similarity between the two series is that the $\delta^{18}\text{O}$ of time-dependent series oscillates around an average value of -26.1‰ which is similar to that recorded for the temperature-dependent series at 350°C and 400°C for 1 hour, -22.4‰ and -28.6‰ respectively.

The decreasing $\delta^{18}\text{O}$ in Runs 2 and 3 are agreement with Run 1. Generally, Run 1 showed higher $\delta^{18}\text{O}$ values in lower temperatures compared to Runs 2 and 3. The latter two data points for Run 3 were not included in the fractionation results (Fig. 7b, Table 3) due to scaling issues in the elemental analyzer. Although individual runs were accompanied by varied analytical precision (+/- 0.5 to 4‰), the trend of decreasing $\delta^{18}\text{O}$ with increasing aging temperature is similar. The NaF reagent was added to the Cu oxide samples in Run 3 (Fig. 7b) to enhance better CO yield in EA, as it is a possibility that poor reproducibility of the isotope analysis in Run 1 (+/- 4‰) was related to incomplete combustion of Cu oxide samples in EA.

Discussion

The Raman measurements presented in this study show that Cu oxidizes readily as Cu_2O is initially formed at lower temperatures and CuO at temperatures above 300°C (Fig. 5) which agrees well with previous studies [63,65]. In the temperature-dependent series, the filling out of the Cu_2O phase and formation of CuO is also supported by the decrease of O vacancies in Cu_2O (147 cm^{-1}) and increase in the main Raman mode of Cu_2O (220 cm^{-1}) [20,64]. The time-dependent series ratio of $147/220\text{ cm}^{-1}$ remains somewhat the same because at a constant temperature of 350°C , the Cu_2O layer is mature, the CuO layer has formed, and the O vacancy concentration has no catalyst to change. Namely, higher reactivity with air in higher temperatures should result in fewer O vacancies.

Diffusion of Cu ions along grain boundaries of Cu_2O is attributed as the mechanism for oxidation in the temperature regime of $200^\circ\text{C} - 550^\circ\text{C}$, so it is expected to see the oxide formation affected by the size of the Cu_2O crystals [63]. The continued oxide growth seen for both series (Fig. 6) is most likely due to the consistency in grain size of Cu_2O , observed through the sustained 220 cm^{-1} Raman peak. For the time-dependent series, the CuO peaks increase and at 3.5 hours, the primary Raman mode of CuO (300 cm^{-1}) dominates over that of Cu_2O (220 cm^{-1}). There is no observed emergence of new peaks in this series, which means that aging time (under the present conditions) has little impact on the type of oxide that grows (Fig. 2), and the increase in 300 cm^{-1} and appearance of 350 cm^{-1} indicates a thickening of the CuO layer. In fact, the Raman spectra reveal markedly similar oxide phases in the time-dependent series samples to the sample of the temperature-dependent series oxidized at 350°C and 400°C for 1 hour. In these samples, the 147 cm^{-1} peak (Cu_2O) is short and broad, while the 220 cm^{-1} peak (Cu_2O) remains sharply defined throughout.

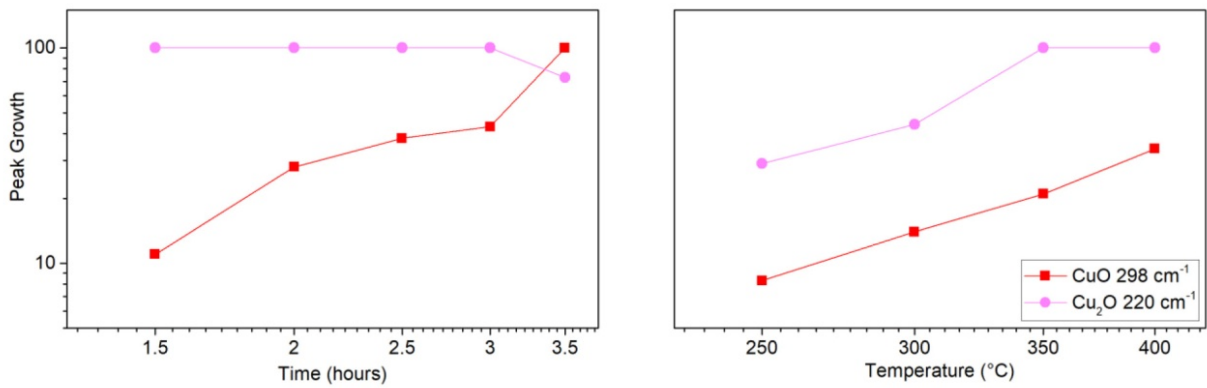


Figure 6: Raman peak intensity of the two primary Raman modes of CuO (298 cm⁻¹) and Cu₂O (220 cm⁻¹) relative to the highest peak for each spectra. Each symbol represents one data point. The lines are included to guide the eye.

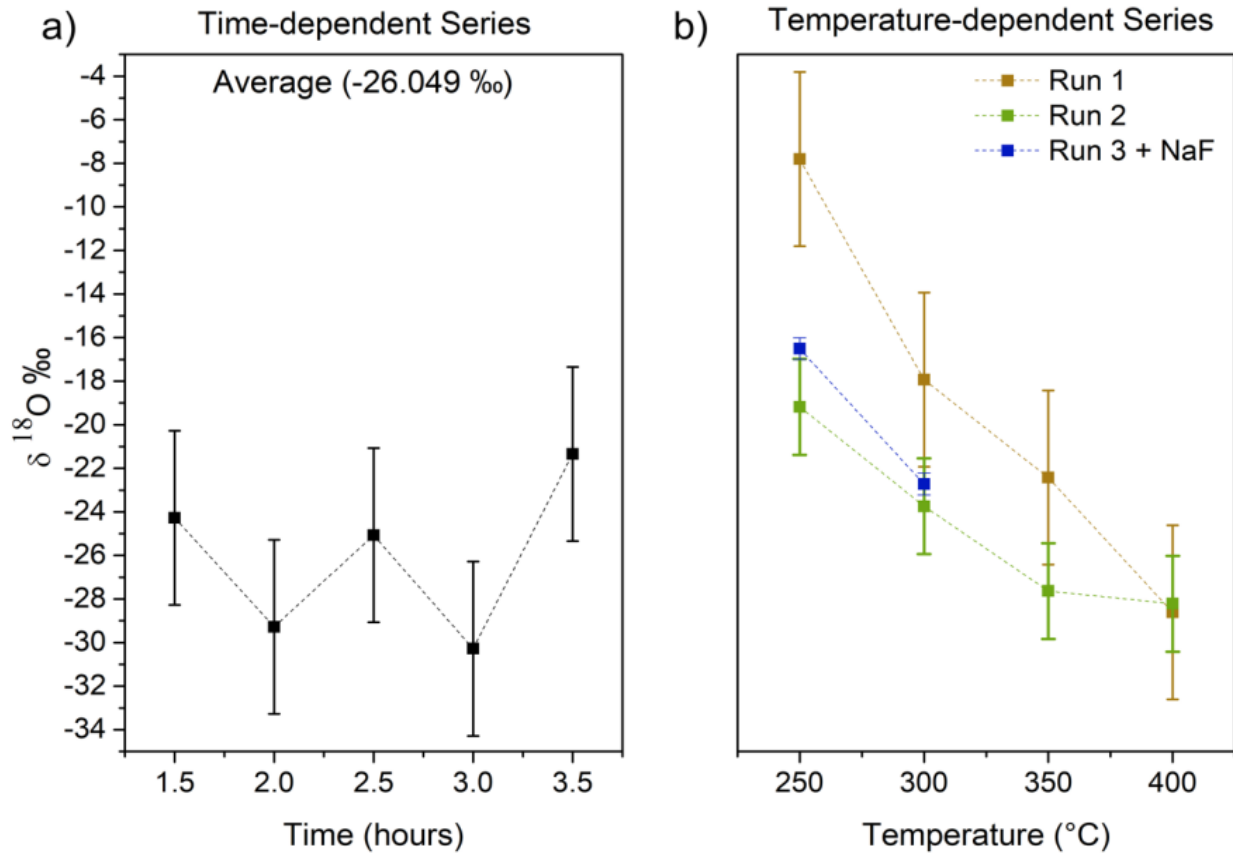


Figure 7: a) Isotope ratio mass spectrometry (IRMS) results of $\delta^{18}\text{O}$ in Cu oxide from samples for the time-dependent series. The error bars are included ($\pm 4\%$). b) IRMS results of temperature-dependent series for the original sample set (Run 1) with two validation sample sets (Runs 2 and 3). Sodium fluoride was added to Run 3 to improve combustion in the IRMS. The error bars are $\pm 4\%$ for Run 1, $\pm 2.2\%$ for Run 2, and $\pm 0.5\%$ for Run 3. Each data point represents an individually aged sample; however, lines are included to guide the eye.

Table 3: Oxygen isotope results for temperature-dependent aging experiments.

Temperature [°C]	$\delta^{18}\text{O} - \text{Cu Oxide [‰]}$			
	Run 1	Run 2	Run 3	Average
250	-7.8	-19.2	-16.5	-14.5
300	-17.9	-23.7	-22.7	-21.5
350	-22.4	-27.6	Off scale	-25.0
400	-28.6	-28.2	Off scale	-28.4

Table 4: Oxygen isotope results for time-dependent aging experiments at 350°C.

Time [hours]	$\delta^{18}\text{O} - \text{Cu Oxide [‰]}$
51.5	-24.3
2.0	-29.3
2.5	-25.1
3.0	-30.3
3.5	-21.3
Average	-26.1

There is evidence of the CuO vibrational overtone at 1130 cm^{-1} as well as distinct peaks for the phase at 297 , 348 , and 630 cm^{-1} [65]. Cu_2O is observed at 417 cm^{-1} and small crystals of an O deficient mixed phase Cu_4O_3 are represented by the broad peak at 510 cm^{-1} (Fig. 5). Not only are these samples comparable through Raman spectra, their O isotope compositions are in agreement as well. The average $\delta^{18}\text{O}$ value of the time-dependent series is -26.1‰ , while the $\delta^{18}\text{O}$ values for the samples of the temperature-dependent series oxidized at 350°C and 400°C for 1 hour are -22.4‰ and -28.6‰ , respectively (Table 3), implying enrichment in ^{16}O isotopes. It is important to reiterate that there is still ^{18}O in the sample; the negative $\delta^{18}\text{O}$ value simply means that there is an increase in ^{16}O uptake with increasing temperature with respect to the sample's isotope composition at lower temperatures.

With increasing temperature, the data reveals peaks moving to the left and sharpening caused by a temperature-induced grain growth within the oxide layer (Fig. 6). This is most apparent with the peak of 1130 cm^{-1} and 630 cm^{-1} , corresponding to CuO and somewhat with the peak of 510 cm^{-1} , corresponding to Cu_4O_3 . However, no peak is detectable at 1130 cm^{-1} in the temperature-dependent series for 250°C and 300°C at 1 hour. Given that the structure of Cu_4O_3 has an upper stability limit ranging from about 400°C to 525°C , the 510 cm^{-1} peak broadens in width and shrinks in intensity at higher temperatures [66,67]. For these reasons, we focus on the peak shift of CuO at 630 cm^{-1} , as it is apparent in all time- and temperature-dependent oxidations (Fig. 8). The overall shift for the samples in the studied temperature regime is dramatic at -19 cm^{-1} whereas the Raman modes of the time series samples seemingly fluctuated resulting in an overall shift of merely -3.4 cm^{-1} . The largest shift is observed between 300°C and 350°C (-16.1 cm^{-1}). The observed shift is triggered by the increase in temperature, into the regime where CuO is more readily formed and thus, more structurally stable [24,63]. Due to scraping off the oxide layer for isotopic analysis in

the IRMS, the measured $\delta^{18}\text{O}$ represents a bulk value of the all Cu oxide layers formed, therefore it is difficult to directly assess the individual influence of Cu_2O vs. CuO on the measured isotopic compositions with confidence. However, analysis of the possible O sources can provide some information on formation mechanisms of Cu oxides in this study. In an experiment conducted by Bernstein [68] which measured O isotope fractionation during the oxidation of copper in dry O_2 gas at < 22 cm Hg, an enrichment in ^{16}O isotopes is observed as in our study (Fig. 5a). His work indicates a distinct decrease of $\delta^{18}\text{O}$ values by ~ 16 to 25% compared to O_2 gas in elevated temperatures (70 to 250°C). Note that on Fig. 5a, the magnitude of this isotope fractionation is shown using a $1000\ln\alpha$ value which is a difference between $\delta^{18}\text{O}$ of Cu oxide and O_2 gas as follow:

$$1000\ln(\alpha)_{\text{Cu oxide} - \text{O}_2} \approx \delta^{18}\text{O}_{\text{Cu oxide}} - \delta^{18}\text{O}_{\text{O}_2}$$

The decrease of $\delta^{18}\text{O}$ is in part due to the reaction being a kinetic process where the light ^{16}O isotopes are reacting at a faster pace compared to heavier ^{18}O isotopes. However, the difference in $\delta^{18}\text{O}$ between Cu oxides and pure O_2 gas measured by Bernstein [68] were contained in a smaller range (~ 16 to 25%) as compared to our study (~ 31 to 53%) carried out in the presence of atmospheric O_2 . Further work by Brown [69] showed that the magnitude of $\delta^{18}\text{O}$ decrease appear to be also controlled to some degree by texture and size of Cu material, involving a varied range of O isotope fractionations (~ 9 to 43%) during Cu oxide formation at temperature range of 1 to 100°C (Fig. 9a). In contrast to previous studies [68,69], our experiments were carried out under a higher temperature range (250 to 400°C), within the growth regime of CuO , and in the presence of air with both atmospheric O_2 and water vapor (moisture) present.

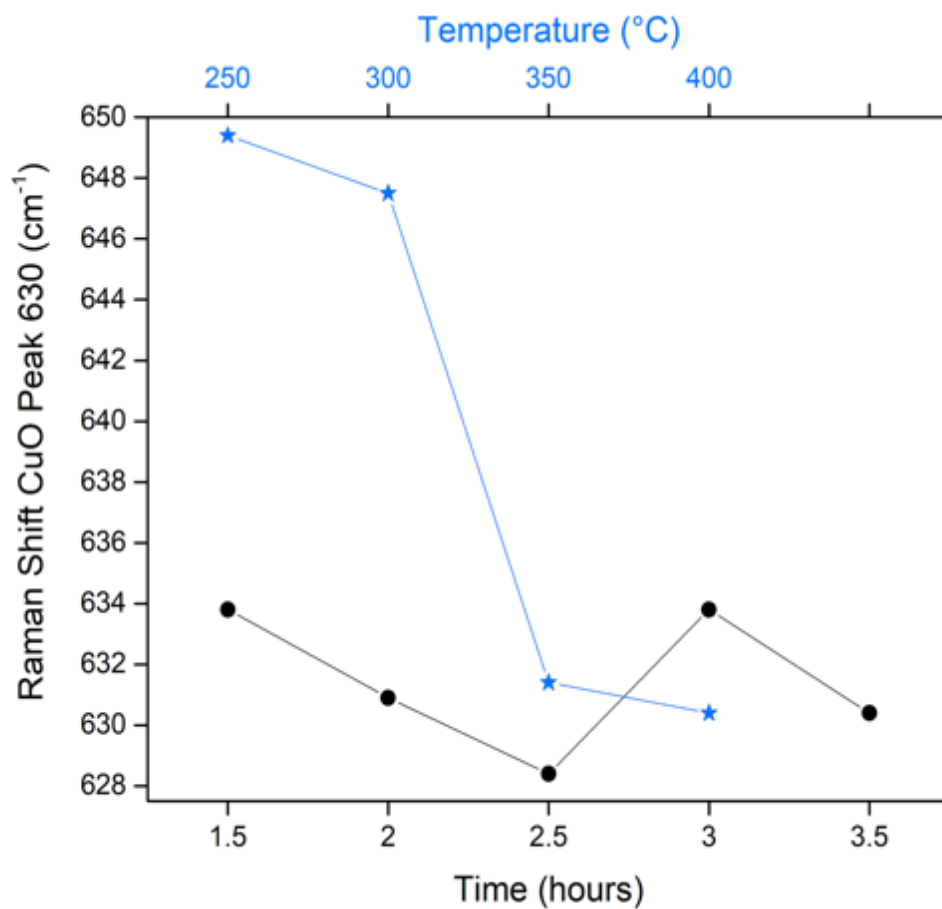
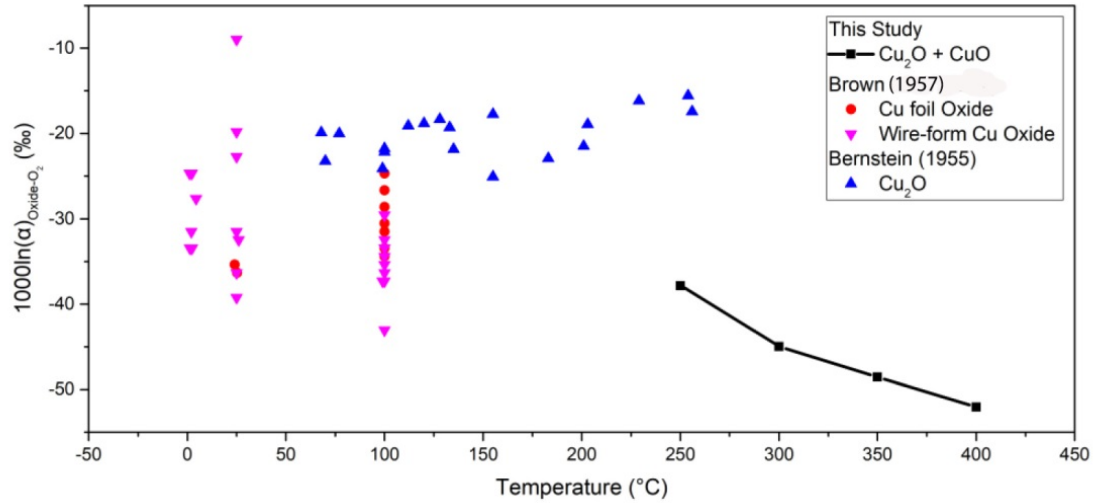


Figure 8: Measured position of the 630 cm⁻¹ Raman mode of CuO as a function of temperature and time.

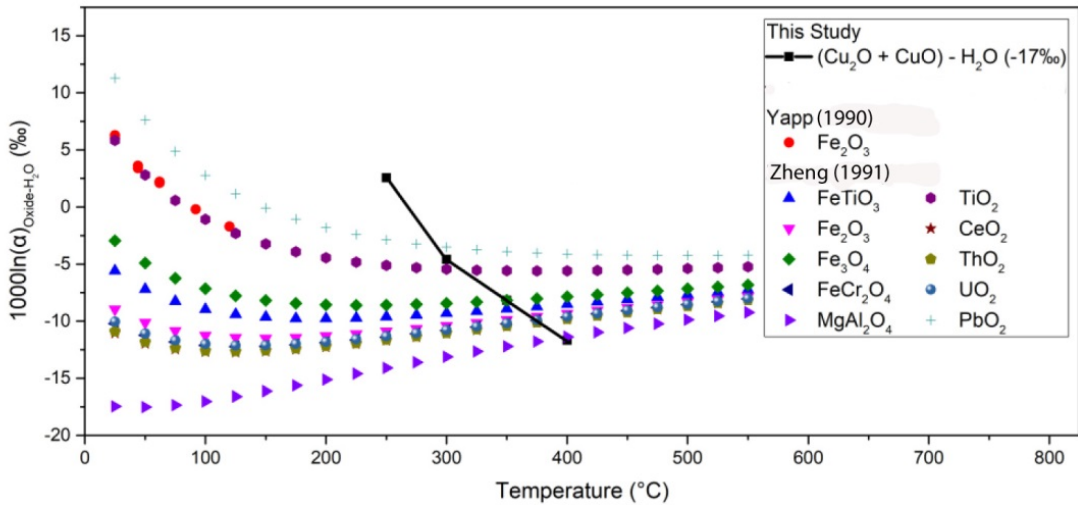
While the results of our study are in general agreement with these earlier studies in pure O₂ environments [68,69], in that the formation of Cu oxides is likely accompanied by enrichment in light ¹⁶O isotopes, the estimated oxygen isotope fractionation (e.g., 1000lnα) between atmospheric O₂ and Cu oxides showed distinctive *negative* correlation with increasing temperature (Fig. 9a). The latter is not apparent in the Bernstein [68] and Brown [69] studies. As shown on Figure 9b, the observed negative correlation between 1000lnα and temperature resembles a similar trend as observed for equilibrium (temperature-dependent) isotope fractionations between various metal oxides and liquid water at lower temperature range of 50-200°C. This suggests that there might be additional O isotope exchange between CuO and water vapor in air after the initial phase(s) of Cu oxide were formed (Fig. 9b), which was absent in the Bernstein and Brown's experiments (Fig. 9a).

On Figure 6, the estimated ranges of δ¹⁸O of Cu oxides are presented using the known O isotope fractionations for reactions with atmospheric O₂ and water vapor (see Fig. 9 for reference). Clearly, the majority of our data falls in the field of O isotope exchange with water, suggesting this process likely controlled the δ¹⁸O of Cu oxides. In our study, the δ¹⁸O of atmospheric O₂ and water vapor were not measured. Thus, the presented isotope fractionations (1000lnα) on Fig. 5ab are theoretical estimates based on the assumed δ¹⁸O for atmospheric O₂ (+23.5 ‰) [70] and water vapor of local precipitation (-17 ‰), and measured δ¹⁸O of Cu oxides (Tables 2, 3).

Although previous studies did not determine the exact fractionations during O isotope exchange between Cu oxides and water, in the studied temperature range (250 to 400°C) the 1000lnα should be increasing with increasing temperature as previously reported for other metal oxides (Fig. 10b) [71].



(a)



(b)

Figure 9: (a-b) Variation of $1000\ln(\alpha)$ as a function of temperature for Cu oxides from this study compared to previously published data for other metal oxides. The fractionation factor, α , is the ratio of heavy to light oxygen isotopes in the metal oxide compared to the ratio of heavy to light isotopes in the oxygen source (atmospheric O_2 on (a) and water vapor on (b)). Note that $1000\ln(\alpha)_{\text{oxide-water}} \approx \delta^{18}O_{\text{metal oxide}} - \delta^{18}O_{O_2/\text{water}}$. For this study, the $1000\ln(\alpha)$ values (in black) were calculated using the measured average $\delta^{18}O$ values of Cu oxides, the known $\delta^{18}O$ of +23.5 ‰ for atmospheric O_2 [70] on (a), and the estimated $\delta^{18}O$ of -17‰ for water vapor on (b) based on the $\delta^{18}O$ of local precipitation of Knoxville, TN. Guide lines are included to lead the eye.

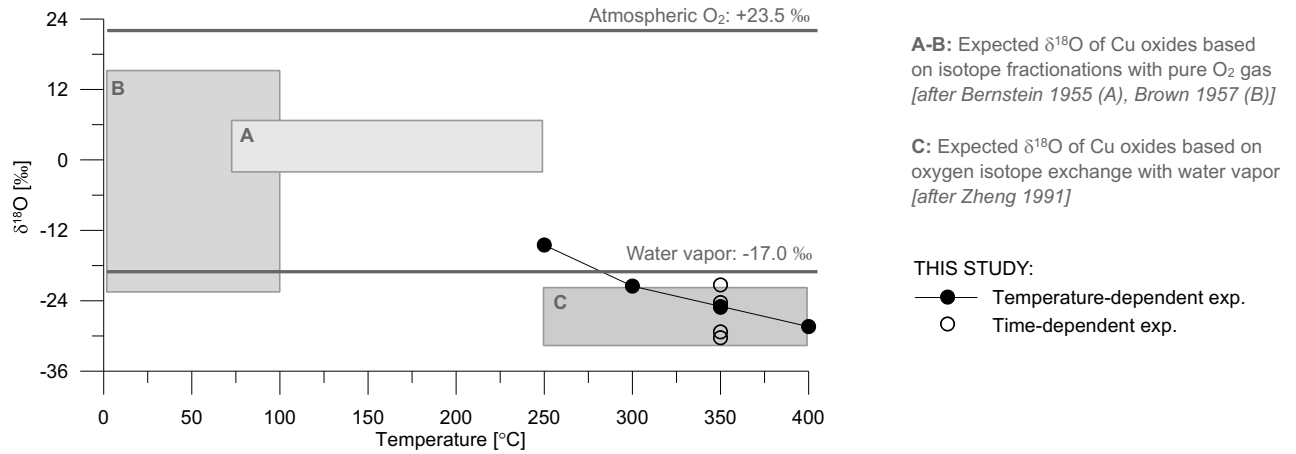


Figure 10: Variation of measured average $\delta^{18}\text{O}$ values as a function of temperature for Cu oxides from this study (black solid and open circles) compared to the $\delta^{18}\text{O}$ values of atmospheric O₂ and water vapor (grey lines), and theoretical ranges of $\delta^{18}\text{O}$ estimated for Cu oxides (gray fields) using isotope fractionations with pure O₂ gas reported by Brown [69] and Bernstein [68] and oxygen isotope exchange between various metal oxides and water reported by Zheng [71].

Generally, a couple of different explanations can be offered to explain the measured discrepancies in the observed temperature-dependent oxygen isotope fractionations. Firstly, it is possible that O isotope fractionations between Cu oxides and water vapor are different than in the presence of liquid water. For example, there is a significant O isotope fractionation between liquid water and water vapor leading to preferential uptake of ^{16}O isotopes into vapor phase [72], which would increase the $1000\ln\alpha$ values presented on Figure 10b particularly in lower temperatures. However, this process would have a minor effect on the $\delta^{18}\text{O}$ of Cu oxides in higher temperatures because O isotope fractionations between liquid water and water vapor are relatively small/negligible (1.6 to 0 ‰) in the studied temperature range of 250 to 400°C, respectively [72]. Secondly, the measured $\delta^{18}\text{O}$ of Cu oxides might represent a subsequent oxygen isotope exchange acquired at the lower temperature range (<200°C) during cooling of the furnace as inferred from the decreasing trends of $1000\ln\alpha$ for varied metal oxides in lower temperatures [73] (Fig. 10b). Note that it took ~1 hour to cool the furnace prior removal of the Cu oxide samples for Raman and isotope analyses, thus the samples were exposed to lower temperatures for the same duration as during the main experiment.

While we are unable to definitely determine the exact temperature of isotope exchange with water vapor in this study, a compilation of our results presented on Figs. 9 and 10 show that there is a distinctive, large O isotope fractionation during formation of Cu oxides in reaction with air (in the presence of both O_2 and water moisture), even larger than in the presence of O_2 only [68,69]. This implies that $\delta^{18}\text{O}$ of oxide materials might be a very useful forensic tool for studying conditions during aging of nuclear materials under natural conditions (e.g., exposure to atmospheric air). Future studies should focus on O isotope exchange between metal oxides and water vapor to better constrain temperature-dependent isotope fractionations that likely affect the $\delta^{18}\text{O}$ of oxide

materials. If successful, this could be used to make potential correlations with climatic/geographic regions, given that the $\delta^{18}\text{O}$ of air moisture is strongly controlled by temperature and local conditions. For example, the $\delta^{18}\text{O}$ of local water vapor varies highly worldwide and is strongly controlled by a distance from equator, altitude and latitude [74]. As the oxidation rate is slower at ambient surface temperatures, the water vapor that is in contact with the metal may be similar to the annual average $\delta^{18}\text{O}$ of water vapor in precipitation [75]. It is expected that regions with dry air may show higher $\delta^{18}\text{O}$ in oxide materials as atmospheric O_2 with higher $\delta^{18}\text{O}$ of +23.5‰ would be mainly used as the oxidant without further significant modification by oxygen isotope exchange with water vapor.

In broad terms, temperature triggers the formation of individual copper oxide phases and the fractionation of O isotopes in air environment, while time determines how much of each oxide phase will form. At 350°C, the time-dependent series already has experienced growth of Cu_2O and a layer of CuO for the uptake of ^{16}O isotopes, as well as the energy in the form of high temperature to induce diffusion of Cu ions through the Cu_2O layer for total oxide growth. For the temperature-dependent series, we see an increase in energy of the system with each increment of temperature, and a new growth regime after 320°C. The CuO phase fully develops, exchanges isotopes with water vapor and thus, more ^{16}O isotopes are incorporated.

Conclusions and Recommendations

A Cu-rich oxide layer (Cu_2O) formed on a Cu metal sample when exposed to air at temperatures ranging from 250 to 400 °C. Above 300 °C, Raman spectroscopy indicated the growth of a second, O-rich phase (CuO). Concurrent to this oxidation process, the $\delta^{18}\text{O}$ of Cu oxides systematically decreased with increasing temperature from -7.8 to -28.6‰. This study demonstrated that the temperature of oxidation determines what type of Cu oxide phase will grow and the magnitude of

oxygen isotope exchange between the maturing oxide phases and water vapor in air. The O isotope fractionation in Cu oxides do not show any significant trend with the thickening of oxide phases at a constant temperature of 350°C (increased time). The main source of O for Cu oxide in this study is most likely water vapor as a result of a subsequent isotope exchange process (e.g., after CuO oxide formation) with moisture in air. Due to local water vapor having extremely distinct, negative $\delta^{18}\text{O}$ values, the IRMS analysis of metallic oxides could be used to determine a location that the oxide has been in for prolonged period of time as well as thermal history of an oxidized nuclear material. While this study focused on accelerated aging, further research under more realistic aging time scales with better controlled environments (varied proportions of O_2 versus water vapor contents, etc.) is needed in order to further improve the interpretation and calibration of this forensic isotopic signature. This technique could be an invaluable asset for applications in nuclear forensics.

CHAPTER 2: STRUCTURAL MODIFICATION OF CU METAL AND CU OXIDE THROUGH ION IRRADIATION (LA-UR-20-24516)

Abstract

Radiation-induced effects and their influence on oxidation processes were evaluated for their use as a forensic tool for special nuclear material (SNM). A beam of 10 MeV Au³⁺ ions were used to mimic the accumulation of microstructural damage from self-irradiation through the decay of radionuclides. Several copper samples were irradiated as suitable surrogate materials at 200 °C with a flux of 1×10^{12} ions/cm²s to damage levels of 5, 10, and 15 displacements per atom (dpa). This corresponds to about 50, 100, and 150 years, respectively, of accumulated α -decay damage in a PuGa alloy assuming a damage rate of 0.1 dpa/year. After irradiation, all samples were exposed to an accelerated aging process induced by thermal treatment at 350 °C for 1 hour in air. This resulted in the growth of a mixed oxide layer (Cu₂O and CuO) which was characterized in detail using several complementary analytical techniques: Scanning Electron Microscopy, Raman spectroscopy, Synchrotron X-ray diffraction (transmission mode), and Grazing Incidence X-ray diffraction. The oxide layer growth of irradiated Cu at 350°C is distinctly modified as a result of the ion irradiation. Most notably, the growth of the CuO phase is suppressed with increasing radiation damage on the Cu substrate, and structural changes occurred in the Cu₂O phase. These results indicate that damage from self-irradiation over time can cause quantifiable modifications in the oxidation process of metals that could be harnessed for their use as a novel forensic tool.

Introduction

The control of Special nuclear material (SMN) and strategic special nuclear material (SSNM), namely Pu, is crucial to national security as the element can be utilized in nuclear explosives [76,77]. Plutonium has a complex phase diagram with many different structure types that form

over a range of temperatures; of interest for the nuclear forensic community is delta-phase Pu, which is stable from 310 °C to 452 °C for pure Pu or can be stabilized at room temperature with addition of ~0.3% Ga. It is of supreme importance that these materials be monitored, studied, and documented for (i) facility accountability and (ii) nuclear forensics and recovery in the event of their diversion from a nuclear facility. Both physical and chemical properties of SNM/SSNM evolve over time due to the decay and transmutation of radionuclides as well as the accumulated damage from self-irradiation [1,2,5]. These changes occur gradually with time and can be correlated with the age of the material for forensic purposes. As mentioned previously, radiochronometry utilizes mass spectroscopy to determine the changes in chemical compositions and ratio of radioisotopes as a measure of the time that has passed since material fabrication [78]. Decay counting techniques based on alpha or gamma emission are in some cases employed to identify specific radionuclides that have formed in a given material [79,80].

Many material identification techniques are currently used for SNM/SSNM with each having some limitations, such as being destructive, requiring large sample quantities (>20g), or being only applicable to certain radionuclides [81]. Nuclear resonance fluorescence (NRF) techniques have been recently explored as nuclear forensic tools as they offer a non-destructive analysis of isotope-specific resonances in a material [82]. While most techniques are based on changes in the chemistry of a material, the use of radiation-damage accumulation as forensic signature is very limited. In geochronology, fission-track dating is an important tool to construct the thermal history of geological and archeological specimens [83]. This technique is based on nanoscale damage trails (tracks) that are induced by spontaneous fission of uranium and thorium, and the density and size distribution are determined by chemical etching and optical microscopy [84]. In a similar way Pu decays over time through alpha decay which creates defects in the material from self-irradiation

[85]. Additionally, Pu metal is subject to surface oxidation when exposed to high temperatures and an oxygen-containing atmosphere [4]. Atomic displacements are generated primarily by collision cascades induced by the heavy recoil nucleus (~ 100 keV) and the alpha particle (~ 5 MeV) at the end of its range [1]. These processes create Frenkel defects (interstitial-vacancy pairs) and helium bubbles from alpha particle accumulation, all of which lead to unit-cell volume swelling, strain, and degradation of thermo-mechanical properties of the material.

Due to the extremely restrictive handling of Pu, Cu is often used as an analogue to study its behavior under various conditions. Motivated by its use in nuclear applications, systematic ion irradiation experiments have been performed over the past decades on Cu, and the radiation damage and its dependence on ion-beam conditions and irradiation temperature are well understood [12-15]. It has been shown that ion irradiation leads to the formation of individual Frenkel defects and defect clusters which depends strongly on the irradiation temperature. Significant changes in the microstructure of Cu are observed for ion irradiation at temperatures of approximately one-third of the melting temperature (T_M) [13]; however, an increased mobility of Cu interstitials at elevated temperatures also leads to efficient damage annealing, resulting in defect recovery where typically $\sim 0.1\%$ of the initially induced defects remain.

Besides radiation damage, oxidation is another important phenomenon that results in chemical changes in SNM. Oxidation mechanisms in Cu are comparable to those of δ -phase Pu in similar environments [85,86] with the formation of an initial Cu-rich oxide phase (Cu_2O) which heterogeneously form in localized sample regions as oxygen adsorbs and coalesces onto the surface. At higher temperatures, the O-rich phase (CuO) readily forms on top of the Cu_2O layer and follows a parabolic growth rate with temperature [86]. How this particular oxidation process in Cu is affected by radiation damage is mostly unknown. In this study, ion-beam experiments are

combined with oxidation studies to gain insight into the effects of radiation damage on the oxide layer growth in Cu under accelerated aging conditions. The complementary analysis reveals distinct changes in the oxide phase fractions that depend on the level of radiation damage.

Experimental Setup

A 99.9% pure, 0.8 mm thick sheet of Cu metal was purchased from McMaster-Carr® and cut into four 6 x 6 mm² squares. Each square was electropolished to remove any residue from sample containment or impurities caused during manufacturing [87]. All ion-beam irradiation experiments were performed at the Ion Beam Materials Laboratory (IBML) at the University of Tennessee. The facility houses a 3.0 MV Pelletron (model 9SDH-2) tandem electrostatic accelerator, manufactured by National Electrostatics Corporation, coupled to three bending ports and endstations [88]. The L3 beamline was utilized and is equipped with the custom-built temperature controlled endstation manufactured by Thermionics Northwest Company. Irradiation experiments were conducted under normal incidence at 2.7×10^{-8} Torr ultrahigh vacuum (UHV). A temperature-controlled manipulator with a 2.5 cm diameter Mo plate fixed with a stainless steel ring served a sample holder system. An external power supply connected to a tungsten filament underneath the Mo plate was used to heat each sample to 200 °C. Three samples were irradiated as a function of increasing fluence as denoted in Table 2, and one sample served as a reference material. The samples were irradiated with 10 MeV Au³⁺ ions at a particle flux of 1×10^{12} ions/cm²/s at a temperature of 200 °C, corresponding to approximately $0.35T_M$ of Cu with T_M being the melting temperature. After irradiation, all samples were rapidly cooled with liquid nitrogen attached to the sample holder and heating filament. The fluence calibration was performed using a Faraday cup placed in the beam behind the sample manipulator [89].

Based on a Pu self-irradiation defect accumulation rate of 0.1 dpa per year, the ion-beam conditions have been adjusted to reach target damage level of 5, 10, and 15 displacements per atom (dpa) in Cu (Table 2). For that purpose, the radiation damage was quantified using the Transport of Ions in Matter (TRIM) package within the SRIM (Stopping and Range of Ions in Matter) program (Fig. 8) [90]. Following a method developed by Stoller *et al.* [28] lattice and binding energies were set to zero in the TRIM calculation and, using the Kinchin-Pease model, the number of Frenkel pairs produced per ion are expressed in accordance to equations 1-3 in the **Pre-detonation Materials** section. After irradiation, 4 Cu samples (pristine, 5 dpa, 10 dpa, and 15 dpa) were subjected to accelerated aging by heating them within an ambient atmosphere to 350 °C for 1 hour using a ramp rate of 10 °C/min in a Carbolite High Temperature Furnace 1800. All samples were heated simultaneously on an alumina plate to minimize temperature uncertainties among different samples. The furnace was switched off after the heating cycle, and samples were allowed to cool to room temperature before removal from the furnace. All samples were stored within an inert nitrogen atmosphere in a glove box before and after irradiation, oxidation, and subsequent structural analysis. Scanning electron microscopy (SEM) was utilized to image the sample surfaces after ion irradiation and prior to oxidation using a Zeiss Dual Beam FIB/SEM. The images were obtained with a 10-keV electron beam using a magnification of 6.3-6.9 kx under 2.2×10^{-6} Torr vacuum. A reduced beam energy and current of 30 kV and 50 pA were selected to minimize further sample alteration or damage annealing by the electron beam. Grazing incidence X-ray diffraction (GIXRD) was performed after irradiation and prior to oxidation using a Panalytical X'Pert3 MRD. The grazing-incidence mode was used due to the shallow depth of the ion-beam damage (Fig. 11). The measurements were conducted using the Cu K- α wavelength of 1.54 Å with a fixed divergence slit of 0.05 mm and continuous scan range of 5° to 70° on all four samples.

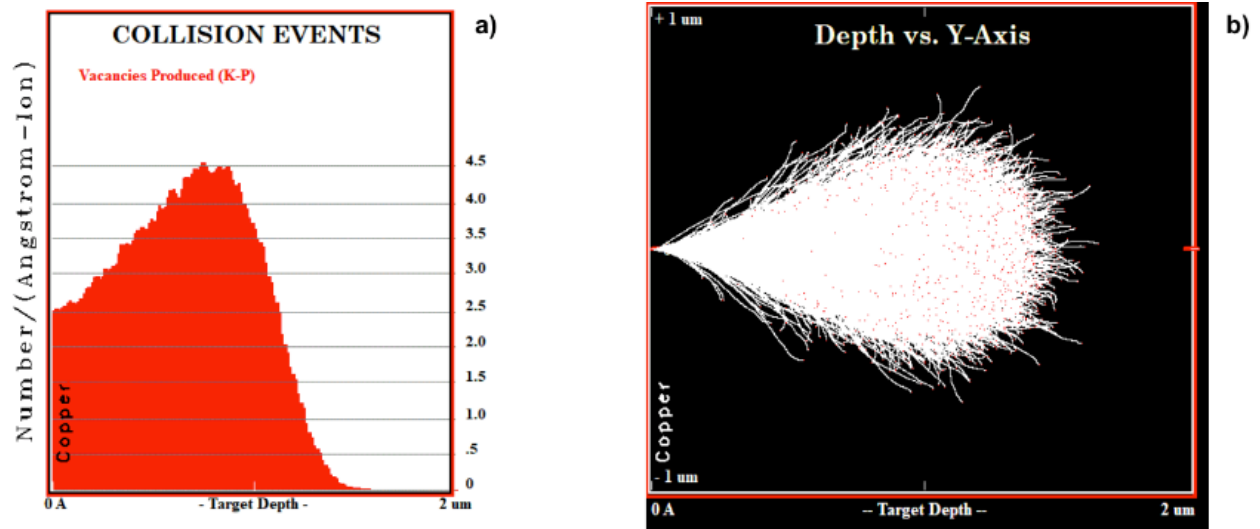


Figure 11: TRIM simulations of 10-MeV Au³⁺ ions in Cu showing (a) the relative damage versus ion penetration depth and (b) the ion range.

The incident grazing angle was 1° , which corresponds to a measurement depth of approximately $0.9 \mu\text{m}$, considering a Cu density of 8.94 g/cm^3 and a packing factor of ~ 1 . This X-ray depth corresponds approximately to the location of the peak damage level as estimated through TRIM calculations (Fig. 11a).

Raman spectroscopy was used to characterize the irradiated samples after oxidation using a high-resolution micro-Raman spectrometer from Horiba (LabRAM HR Evolution) equipped with liquid nitrogen-cooled charge-coupled device (CCD) (Symphony). The measurements were performed with a green laser (532 nm) at a magnification of $50\times$ and power setting of 7.95 mW to avoid laser-induced damage or heating. A two-dimensional Raman spectra map was recorded across each copper oxide surface utilizing a $100 \mu\text{m}^2$ grid with 600 gr/mm and two accumulation steps each at 120 s . These map measurements were taken in the center of the samples to eliminate bias from nonuniformities around the edges. The software package Lab Spec 6 was employed to collect and analyze all Raman spectra.

Finally, the oxide layer on each copper sample was carefully scrapped off with a dull needle and crushed into a fine powder. The resulting powder was loaded into microscopic sample holders consisting of $100 \mu\text{m}$ holes drilled into a $25\text{-}\mu\text{m}$ thin molybdenum foil. Synchrotron-based X-ray measurements were performed at the HPCAT sector at beamline 16 BM-D at the Advanced Photon Source of Argonne National Laboratory [44]. A highly-focused X-ray beam (spot size: $\sim 25 \mu\text{m}$) was used for diffraction measurements in transmission mode to study the oxide samples pressed into the microscopic sample chambers. This approach was originally developed for irradiated powder samples and sample-holder preparation and X-ray measurement procedures are described in detail elsewhere [44]. The measurements were performed using a 30 keV X-ray beam and a MAR345 CCD detector in air at ambient temperature using exposure times of 300 seconds . The

resulting 2-D diffraction images were integrated into 1-D 2θ -intensity profiles (XRD patterns) with the Dioptas software [91] which were analyzed by Rietveld refinement [92] using GSAS-II software [93] to obtain unit-cell parameters and establish fractions of the different copper-oxide phases.

Results and Discussion

GIXRD was used to analyze the effect of ion irradiation in the Cu metal as a function of increasing dpa level (Fig. 12). The X-rays from the utilized GIXRD setup penetrated to a depth of 0.86 μm , which was larger than the peak-damage level ($\sim 0.75 \mu\text{m}$) but smaller than the ion range was ($\sim 1.5 \mu\text{m}$). Thus, the XRD patterns are representative of the damage layer induced by the 10-MeV Au ions in Cu. The two diffraction maxima (111) and (200), which are apparent in the pristine and all irradiated samples were fitted using a Pseudo-Voigt profile (Fig. 12).

Peak positions and widths remain unchanged within the uncertainties and only the peak-intensity show variation among the series. While the intensity of (111) and (200) are similar in the pristine sample and after irradiation to 5 dpa, the (200) maximum is lower in intensity for the 10 dpa samples and the opposite trend is observed after irradiation to 15 dpa. The notable reduction in peak intensity of the (200) peak at 10 dpa is unusual and difficult to confirm with existing literature. The changes in peak intensities may be related to defect accumulation and saturation with increasing dpa level, but texture effects in the Cu samples may also explain the behavior of peak intensities.

There is no evidence of oxide phases in the XRD patterns that may have occurred during irradiation or sample handling in air. Irradiation effects in Cu have been studied in great detail [94-97], and under present irradiation conditions using 10-MeV Au ions and an irradiation temperature of 200 $^{\circ}\text{C}$, only a small Cu vacancy concentration of $<0.1 \text{ at.}\%$ is expected even at 15 dpa due to

recombination and annealing of defects during irradiation and cooling [96]. Defect loss scales with ion fluence as more localized thermal zones created by an increase of incident ions triggers destabilization of previously formed defect clusters [97]. Defect production is initially triggered through cascade events, creating Frenkel pairs and defect clusters. As the irradiation time increases, these defects undergo a variety of transformations – most notably, to stacking fault tetrahedra (SFT) with the formation and subsequent collapse of dislocation loops [97,98]. SFT are highly stable defects and their annihilation requires high temperature annealing (beyond the irradiation temperature used here). Due to the high defect recovery and small amounts of surviving defects in Cu under the present irradiation conditions, no significant structural changes are expected that are readily observable by XRD experiments.

The oxidation of Cu proceeds with molecular oxygen that initially dissociates on the metal surface, producing a string of Cu-O-Cu-O clusters [10-11, 24, 63]. These pre-cursors result in the formation of the Cu-rich Cu₂O phase in these oxide islands, or nodules, whose growth is facilitated through O diffusion across the Cu surface. Excess O at the Cu₂O-air interface creates Cu vacancies by bonding with two electrons, generating a concentration gradient through which the mobile Cu ions are forced by the electric field between the Cu and chemisorbed O. This process is described by the Wagner model which attributes oxidation to the diffusion of ions in a system that is electrically conductive - in this case Cu¹⁺ to the Cu₂O/O₂ interface - driven by the decreasing concentration of Cu vacancies from the surface (air) to the metal (Cu) [10-11, 24, 63]. Concurrent with the migration of Cu vacancies toward the oxide/metal interface, O vacancies are formed and migrate to the oxide/air interface where they annihilate with O in air. The rate limited step of oxidation is by diffusion through this oxide layer once the initial Cu₂O nodules have coalesced.

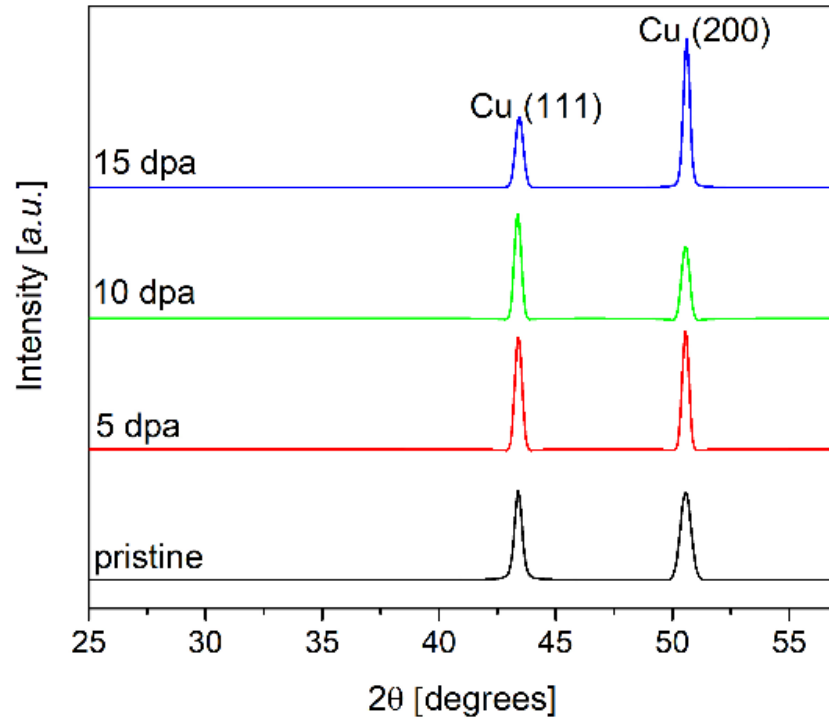


Figure 12: Grazing incidence XRD patterns of pristine and irradiated Cu metal. The patterns are stacked for increasing level of radiation damage expressed as displacements per atom (dpa). The two diffraction maxima are indexed for the sample irradiated to 15 dpa.

Once a connected Cu₂O layer has formed CuO will begin to grow on top if the temperature exceeds 320°C (Fig. 13a). Given the accelerated aging conditions utilized in this study (350 °C, air) both Cu-oxide phases are observable with the Cu₂O being much more abundant than CuO (Fig. 13b) in the XRD data. The synchrotron X-ray measurement was performed on the entire bulk oxide layer which was scrapped off the sample and represents therefore mostly the buried Cu-rich oxide phase. In contrast, the Raman spectra are representative of only the most upper layer of the (unremoved) oxide which is dominated by the CuO phase. The synchrotron XRD pattern of Cu₂O is in good agreement with literature data [10], but the CuO phase is difficult to analyze and is only detectable by the (002) and (-202) the two very low intensity diffraction maxima (Fig.13b). The Cu₂O phase is apparent in the Raman spectrum by the dominant mode at 220 cm⁻¹. There is an additional peak at 147 cm⁻¹ explicitly related to a defective Cu₂O phase (characterized by Cu vacancies).

Because the Raman is more representative to the upper sample regions – this peak could be indicative of the transition zone from Cu₂O to CuO revealing the Cu₂O phase that becomes increasingly Cu vacancy rich until it forms CuO. The spectrum is dominated by the intense 298 cm⁻¹ mode of CuO with additional modes of this phase at about 345 cm⁻¹ and 630 cm⁻¹.

The data of the oxide layers that form on the unirradiated reference sample after accelerated aging will serve as benchmark to identify effects from ion irradiation. As discussed above, the damage in the Cu samples is expected to be subtle with small amounts of simple defects and defect clusters. Point defects on the Cu surface may create adsorption sites, that lead to an enhanced oxidation kinetics [99]. The oxidation kinetics could be similarly affected by more complex defect clusters and associated strain fields. It can be expected that radiation damage impacts the oxidation process mostly at the oxide/metal surface and less towards the oxide/air boundary.

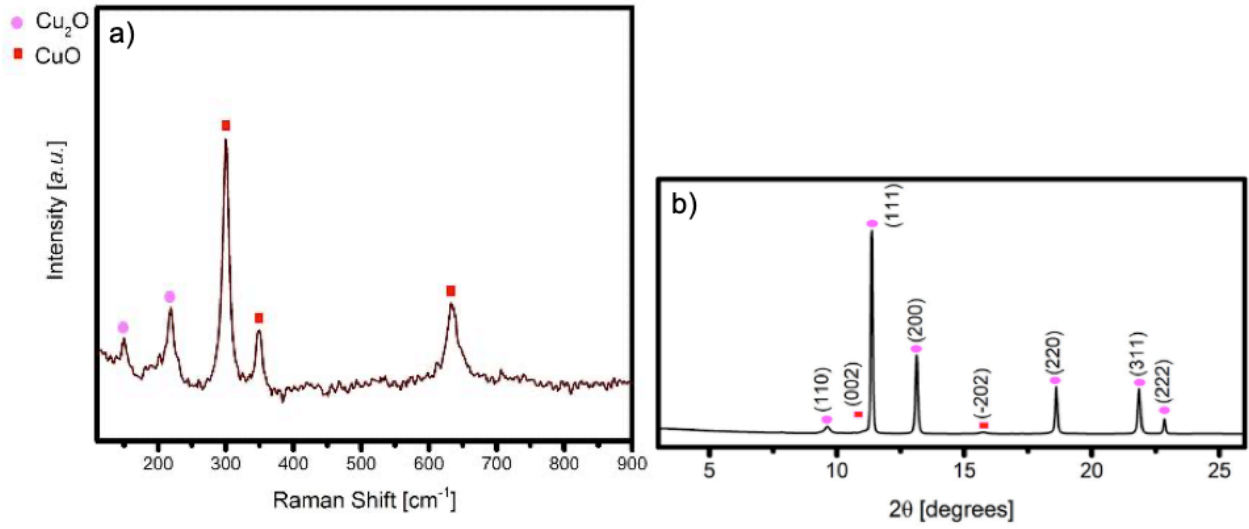


Figure 13: (a) Raman spectrum and (b) synchrotron XRD pattern of pristine Cu oxidized at 350 °C within an ambient air furnace for 1 hour. The growth of the two Cu oxide phases (Cu₂O marked with pink dots and CuO marked with red squares) is confirmed by both techniques. The XRD pattern in (b) is indexed for both phases.

With increase in oxide layer thickness for extended aging time, the effect of radiation would become less pronounced. Previous studies showed that irradiation effects can have a profound effect on oxidation. For example, oxidation of pre-irradiated zircaloy (300 keV protons to a fluence of 10^{18} ions/cm² at a temperature of 350°C) showed variation in the phase fraction of ZrO₂, with the tetragonal phase being suppressed when oxidized at 360°C [100]. In the case of Cu, irradiation may have a similar effect on the Cu-oxide phase fractions which can be analyzed by measurements of irradiated and aged samples similar as shown in Fig. 13 for the reference sample.

The Raman spectra of oxidized irradiated Cu indicates that the initially dominating CuO phase in unirradiated Cu (Fig. 13a) is suppressed with increasing damage level (Fig. 14a) in agreement with the aforementioned study [100]. The most intense mode of CuO at 298 cm⁻¹ significantly decreases in intensity with irradiation, broadens and merges with the 350 cm⁻¹ mode. The third CuO mode at 630 cm⁻¹ behaves similarly to the 350 cm⁻¹ mode with peak broadening and intensity reduction which become more pronounced with irradiation (Fig. 14a). However, the mode at 298 cm⁻¹ appears to be most impacted by irradiation with an intensity reduction that is more significant as compared to the other two modes. The position of the three CuO modes remain remains constant but all peaks shift with a similar behavior to lower wavenumbers in the oxide grown on the 15 dpa sample (Fig. 15a). To obtain an estimate on the fraction of the two Cu-oxide phases, the ratio of the two most intense Raman modes (298 cm⁻¹ for CuO and 200 cm⁻¹ for Cu₂O) was compared for the 5, 10, and 15 dpa sample (Fig. 15b). With increasing damage level, the CuO phase linearly decrease and the Cu₂O becomes the dominating oxide phase in the near surface region characterized by Raman spectroscopy. After irradiation, a new Raman mode becomes apparent at 417 cm⁻¹, which can be associated with a two-phonon coupling effect in Cu₂O [58, 101-102]. This behavior remains unclear but indicates that irradiation effects are also present in the Cu₂O phase.

The other Raman modes of Cu₂O, most noticeably the main mode at 220 cm⁻¹, remain for the most part unchanged when comparing the spectra of the irradiated and reference samples. There is also no notable effect of radiation apparent in XRD patterns of Cu₂O (Fig. 14b). The CuO phase remains detectable up to 15 dpa but the overall small amount makes it difficult to quantitatively assess changes in the phase fraction similar to that in Raman spectroscopy. The only distinct modification in the XRD pattern is the decrease in intensity at 10 dpa in the (200) reflection (Fig. 14b). This is similarly observed in the irradiated Cu sample prior to accelerated oxidation and can be attributed to texture effects [59]. The Cu₂O phase grows epitaxially onto the Cu surface, resulting in the morphology and surface effects present on the metal translating directly to the initial oxide layer growth.

The Raman and XRD analysis show that irradiation impacts mostly the oxide layer close to the oxide/air surface by suppressing the growth of CuO with increasing damage level. This behavior is unexpected but can be explained by defects (or associated strain fields) in the Cu metal which affect during accelerated aging diffusion processes and the growth of CuO.

It has been demonstrated that in other materials (*e.g.*, Pt(110)), where oxidation does not occur on a pristine surface, ion irradiation and associated defects create adsorption sites that stimulates oxygen adsorption [101]. An alternative explanation is that irradiation directly impacts the initial growth of Cu₂O oxide nodules in the irradiation chamber. Oxidation of Cu proceeds *via* nucleation and growth of oxide islands under low oxygen partial pressure and high temperature, an environment similar to that of the irradiation chamber utilized in this experiment [103,104]. Additionally, SEM analysis of the pristine and irradiated Cu sample prior to accelerated aging shows small circular-shaped surface defects which may represent Cu₂O nodules that appear to coalesce with increasing fluence (Fig. 16).

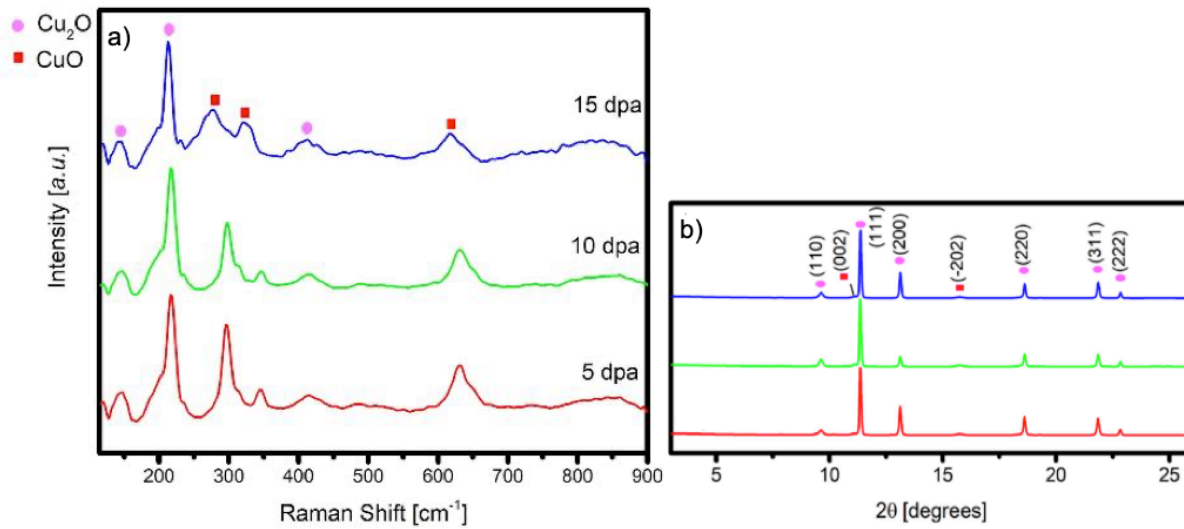


Figure 14: (a) Raman spectra and (b) synchrotron-based XRD patterns of irradiated Cu (10-MeV Au, 5, 10, and 15 dpa) after oxidation at 350 °C within an oxygen atmosphere. The two Cu oxide phases, Cu₂O and CuO, are marked with pink dots and red squares, respectively.

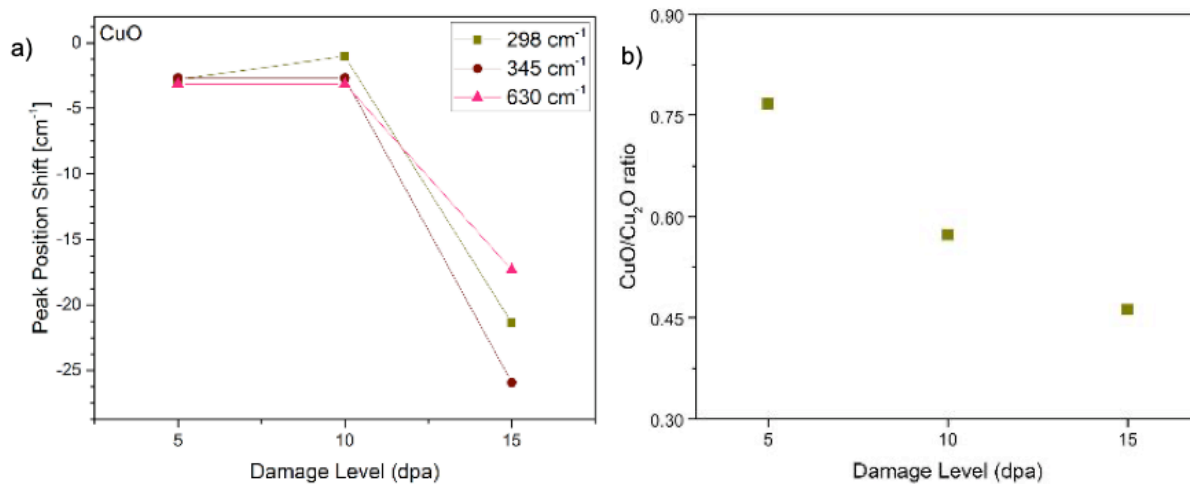


Figure 15: (a) Raman peak shift of CuO with respect to Cu₂O 220 peak [cm⁻¹] and (b) Raman peak intensity ratios of the 298/220 cm⁻¹ modes representative of CuO and Cu₂O, respectively. Each data point represents the peaks in labeled sample spectrum.

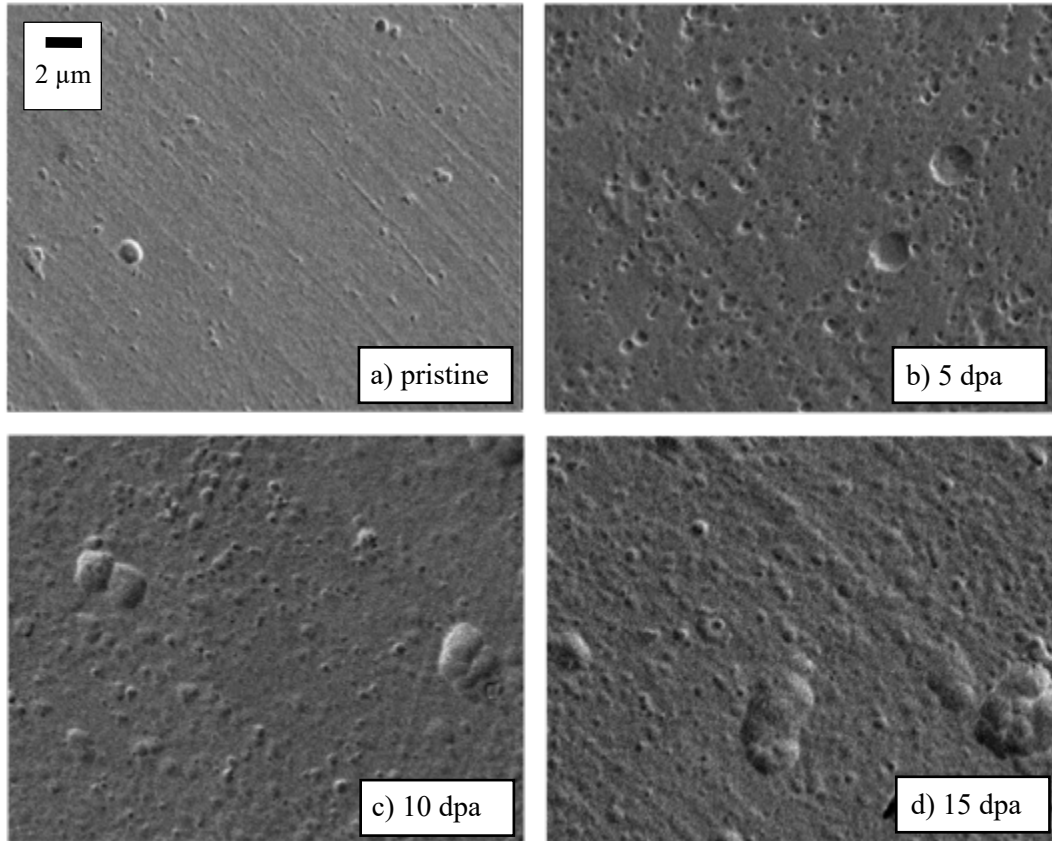


Figure 16: SEM images of pristine Cu metal (a) and Cu metal irradiated with 10 MeV Au³⁺ ions to 5 dpa (b), 10 dpa (c), and 15 dpa (d).

These surface features may represent Cu_2O nodules and the evolution under irradiation may indicate ion-beam induced modifications in this precursor oxide phase. Thus, the observed changes in the oxide phases due to irradiation can be understood by two processes: (i) structural changes in the initial Cu_2O formation on the metal surface due to increased adsorption sites by defects at the Cu surface and/or modification of diffusion processes due to these defects and (ii) radiation effects in the precursor Cu_2O nodules that alter the growth of CuO under subsequent accelerated aging. The Cu-rich Cu_2O phase can incorporate considerable amounts of O in its structure before transitioning to CuO , demonstrated by bulk O/Cu ratios up to 0.67 [105].

Thus, if irradiation in the chamber induces Cu vacancies in the Cu_2O nodules and this translates under further growth during accelerated aging, there can be significantly more O intake in Cu_2O before CuO forms, which would corroborate the suppression of the latter phase with increasing fluence. Which of the two processes is driving the changes in the Cu oxide phases cannot be discerned and further studies are required to fully understand the underlying mechanisms. However, irradiation has a clear effect on the oxidation growth and the fraction of Cu_2O and CuO phases can be linked to the irradiation dose.

Thus, if effects are similar under the conditions of self-irradiation in SNM these changes in the oxidation process could be linked to the thermal history of the material and can serve as independent forensic tool. In SNM, self-irradiation occurs alongside with oxidation over time and, similar to this study, defects in the metal (or alloy) and in the oxide itself may alter the aging process and resulting oxide phases. Raman spectroscopy showed most clearly these changes which is an important consideration for nuclear forensic as recent development has resulted in simple hand-held devices that can be easily employed in the field.

Conclusions and Recommendations

This study utilized Cu as surrogate for special nuclear materials to study the effect of self-irradiation on oxidation processes. The accumulation of self-irradiation was simulated by ion-beam experiments using a 10-MeV Au ion beam at 200 °C to damage levels of 5, 10, and 15 dpa and oxidation was accelerated by heating the samples within an ambient atmosphere to 350 °C. The expected radiation damage in Cu under the applied conditions are point defects, dislocation loops, and stacking fault tetrahedra with an overall concentration of <0.1 at.%. Raman spectroscopy and XRD experiments showed modifications in the oxide layers and most notably a distinct change in the phase fraction with increasing irradiation. The outer CuO phase which forms on Cu₂O was increasingly depleted with damage accumulation. This can be explained by irradiation-induced defects (and associated strain) that serve as additional adsorption sites modifying the morphology of the initial Cu₂O phase that forms directly on Cu. These defects may impact also diffusion process that can also alter the oxidation behavior.

However, while the main oxidation occurs during accelerated aging at 350 °C in air, precursor Cu₂O nodules form already in the irradiation chamber and are also exposed to the ion beam. SEM analysis showed a clear evolution of the Cu surface morphology prior to accelerated aging. The radiation damage in these initial Cu₂O oxide islands can also impact subsequent oxidation leading to the depletion in CuO in surface regions of the heavily irradiated Cu samples. Similar processes may occur during oxidation of δ -phase Pu with accumulated radiation damage from self-irradiation and structural modifications in the oxide layer may be harnessed as a forensic signature.

POST-DETONATION MATERIALS

Nuclear debris, resultant in the event of a nuclear detonation, undergoes a complex formation process. At time zero, the nuclear device is deployed. In a short time following, this device detonates producing a mass ejection of both neutrons and x-rays, pushing out a fireball and wall of immense pressure. When the pressure and shock wave connect with the ground, part is reverberated upward after impact sending with it a large amount of earth with it. The temperature in this cloud of mixed debris is anywhere from 5000 to 20,000 K, melting virtually all elements and mixing them in a turbulent, radioactive plume. When this mixture cools, which takes place over multiple time scales, it settles in the form of bead and tear-drop shaped glasses. The task once this process finalizes is to accurately identify from those glasses what type of device was used and where did the material originate from [106]. In pursuit of characterizing these materials, inductively coupled plasma-mass spectrometry (ICP-MS) is often employed to obtain high fidelity measurements of specific elements and their concentrations. In reality, when conducting these measurements, the user is really measuring isotopes while assuming their natural abundances. ICP-MS requires the sample to be in liquid form, which often involves a digestion process accomplished by the use of an acid. It is more difficult to measure elements that tend to form negative ions such as Cl, I, and F due to their ionization energy. This is one limitation of using ICP-MS – it is capable of detecting any element, but in order to get the elements through the instrument relies heavily on their ability and ease of ionization. Other limitations of ICP-MS come in the form of interferences, which can either be related to the environment or the analyte and spectrometric processes themselves. These involve isobaric, polyatomic/adduct ion, and doubly charged ion interferences. It should be noted that sending samples from the site back to an equipped laboratory for non-destructive and destructive analysis (NDA and DA, respectively) is still an

incredibly critical step of nuclear forensics, integrated to provide unparalleled information on these samples. However, the scope of this research on nuclear melt glass focuses on the first line of analysis and identification.

Nuclear Underground Engineered Test Surrogates (NUGETS)

In order to obtain accurate measurements on the composition of melt glass, it is often sent back to a laboratory for measurement through a table top mass spectrometer such as an Inductively Coupled Plasma Mass Spectrometer (ICP-MS). This process yields reliable results but sacrifices precious time. Some decay products have half-lives on the order of minutes which would not be detected by the time the sample is transported back to a proper facility [106]. The focus in post-detonation nuclear forensics is currently to develop novel techniques for on-site characterization. Over the past decade, great strides have been made in the replication of this glassy fallout for use in pinning down advanced characterization methods [107]. Boone, Auxier, Seybert, Molgaard, etc. have formulated a method for reproducing this slurry dependent on location of detonation. They have been successful at producing synthetic glasses for trinity site [108], New York, New York and Houston, Texas [109] as well as glasses representative of underground detonation at the Nevada test site [110]. In addition, there have been preliminary studies focused on urban/marine environments [111]. This study utilizes the Nuclear Underground Engineered Test Surrogates (NUGETS, NV1X series Fig. 17). Composition of these melt glasses are found in Table 5. For explicit methodology on the mathematical formulation of the synthesized components the reader should refer to Boone [110]. The NV1X series were formed through firing in a furnace. NV1A and NV1B were fired below the liquidus point at 1500°C for 30 minutes while NV1C was fired at 1600°C for 35 minutes and NV1D at 1570°C for 30 minutes. This is to simulate the variety of thermal exposure to the soil and replicate melt glass in different locations.

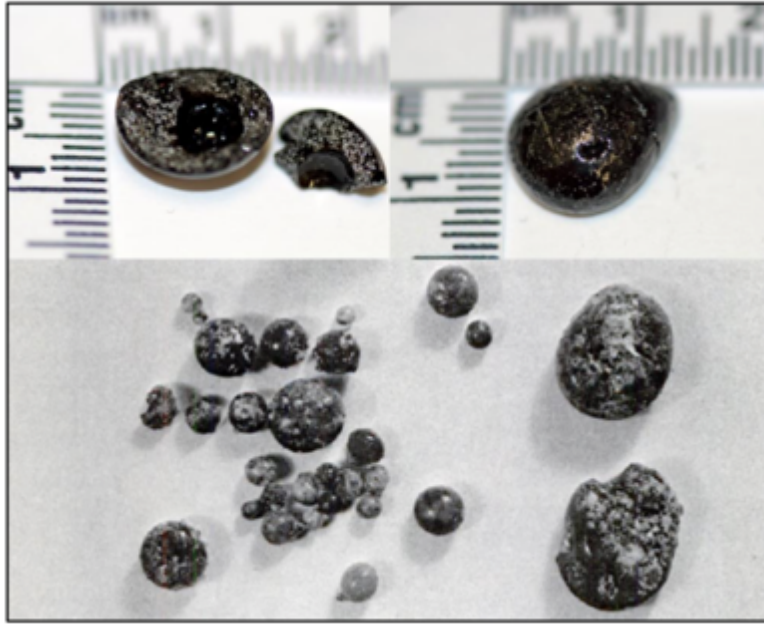


Figure 17: NVIC Sample bottom side (top left) and reflective side (top right) as compared to underground nuclear explosive melt debris (U-NEMD).

Table 5: List of NUGET NV1X samples compositions (wt%)

Oxide	Composition
SiO ₂	71.27
Al ₂ O ₃	14.36
TiO ₂	0.34
Fe ₂ O ₃	2.48
MgO	0.75
CaO	3.58
NaOH	1.52
KOH	5.38
MnO	0.07
Ca ₃ (PO ₄) ₂	0.26

Specifically, for underground nuclear melt glass, the elemental composition is majorly constrained to the host geochemistry but will also include elements representative of the device components, activation products, and fission products dependent on the type of fuel [110].

In pursuit of characterizing these materials, inductively coupled plasma-mass spectrometry (ICP-MS) is often employed to obtain high fidelity measurements of specific elements and their concentrations. In reality, when conducting these measurements, the user is really measuring isotopes while assuming their natural abundances. ICP-MS requires the sample to be in liquid form, which often involves a digestion process accomplished by the use of an acid. It is more difficult to measure elements that tend to form negative ions such as Cl, I, and F due to their ionization energy. This is one limitation of using ICP-MS – it is capable of detecting any element, but in order to get the elements through the instrument relies heavily on their ability and ease of ionization. Other limitations of ICP-MS come in the form of interferences, which can either be related to the environment or the analyte and spectrometric processes themselves. These involve isobaric, polyatomic/adduct ion, and doubly charged ion interferences. It should be noted that sending samples from the site back to an equipped laboratory for non-destructive and destructive analysis (NDA and DA, respectively) is still an incredibly critical step of nuclear forensics, integrated to provide unparalleled information on these samples. However, the scope of this research on nuclear melt glass focuses on the first line of analysis and identification.

Environmental Standards

Utilizing standards as a means of comparison for the chemical characterization techniques proposed in this document is critical for validation of results. Particularly, when studying synthesized materials that were not manufactured by an accredited company such as the aforementioned NUGETS, comparison to a known composition is mandatory. In the procedures

outlined below, NUGETS samples are compared primarily to the National Institute of Standards and Technology (NIST) Standard Reference Material (SRM) 610 standard [112]. This standard has a known composition (Table 6) and has been used in previous studies as an acceptable comparison for nuclear melt glass due to its trace amounts of uranium and other fission products [113,114]. In addition to this standard, in the formulation of the Partial Least Squares Regression (PLSR) code detailed in the sections below, a number of standards between 20-30 are used (Table 7). These are from the same source of those utilized for the calibration of the ChemCam on Mars [115,116]. These samples contain at least 5 compositions higher and lower than the specified NUGET compositions (except for K_2O , which is difficult to find standards with high concentrations).

Experimental Methodology

NUGETS synthesis

From [110], the samples were fired in a CM Furnaces 1700 Series Rapid Temp Lab Furnace capable of executing a 12-segment heating profile where each odd numbered segment executes a temperature increase at a programmed rate [$^{\circ}C/min$]. The even segments allow dwell times at the temperature set point for a programmed amount of time. High-purity (2 ppm total impurity content) graphite crucibles sourced from SPEX Sample Prep were used in the firing of NUGETS. These materials were measured with analytical balances with a resolution of $0.1\text{ mg} \pm 0.2\text{ mg}$ in separate weigh boats. After weighing each chemical constituent, they were placed in a standard ceramic laboratory mortar where it is ground by hand with a ceramic pestle until the powder is homogeneous. There were minor problems reported in the preparation of NaOH and KOH pellets due to humidity.

Table 6: NIST 610 Compositional Values (wt%)

Element	NIST610
Al	1.06
Ca	8.58
Fe	0.05
K	0.05
Mg	0
Mn	0.05
Na	10.39
Si	33.66
Ti	0.04

Table 7: Geological Standards utilized for analytical comparison and model formation.

Sample	SiO ₂	TiO ₂	Al ₂ O ₃	Fe ₂ O ₃ T	MnO	MgO	CaO	Na ₂ O	K ₂ O	P ₂ O ₅
AGV2	59.30	1.05	16.91	6.69	0.10	1.79	5.20	4.19	2.88	0.48
BCR2	54.10	2.26	13.50	13.80	0.20	3.59	7.12	3.16	1.79	0.35
BEN	38.20	2.61	10.07	12.90	0.20	13.15	13.87	3.18	1.39	1.05
BHVO2	49.90	2.73	13.50	12.30	0.17	7.23	11.40	2.22	0.52	0.27
BIR1	47.70	0.97	15.40	11.33	0.18	9.70	13.40	1.81	0.03	0.03
BK2	58.83	1.94	14.77	8.78	0.19	2.82	4.64	3.35	3.99	0.71
BT2	48.57	1.52	16.46	11.09	0.15	6.42	7.92	4.48	1.28	0.44
GBW07103	72.83	0.29	13.40	2.14	0.06	0.42	1.55	3.13	5.01	0.09
GBW07113	72.78	0.30	12.96	3.21	0.14	0.16	0.59	2.57	5.43	0.05
GBW07311	76.26	0.35	10.37	4.78	0.32	0.62	0.47	0.46	3.27	0.06
GBW07312	77.29	0.25	9.30	6.20	0.18	0.47	1.16	0.44	2.91	0.05
JR1	75.41	0.10	12.89	0.89	0.10	0.09	0.63	4.10	4.41	0.02
UNSZK	74.38	0.04	14.19	1.75	0.03	0.07	0.43	4.50	4.06	-
GBW07104	60.62	0.52	16.17	4.90	0.08	1.72	5.20	3.86	1.89	0.24
GBW07114	0.58	0.02	0.09	0.21	0.01	21.64	30.00	0.03	0.04	0.01
GBW07217A	0.95	-	0.29	0.38	0.06	20.91	30.67	0.02	0.00	0.00
GBW07110	63.06	0.80	16.10	4.72	0.09	0.84	2.47	3.06	5.17	0.36
NAU2	48.70	0.60	4.53	31.76	0.02	0.77	1.96	0.70	0.13	-
JA2	56.42	0.66	15.41	6.26	0.11	7.60	6.29	3.11	1.80	0.15
JA3	62.26	0.68	15.57	6.59	0.11	3.65	6.28	3.17	1.41	0.11
SWY1	62.90	0.09	19.60	3.71	0.01	3.05	1.68	1.53	0.53	0.05
JB1B	51.11	1.26	14.38	9.01	0.15	8.14	9.60	2.63	1.32	0.26
JB2	53.20	1.19	14.64	14.34	0.20	4.66	9.89	2.03	0.42	0.10
JB3	51.04	1.45	16.89	11.88	0.16	5.20	9.86	2.82	0.78	0.29
JA1	63.97	0.85	15.22	7.01	0.16	1.57	5.70	3.84	0.76	0.17
GUWGNA	71.47	0.02	14.70	5.92	0.17	0.03	0.62	0.08	2.63	0.00

Amounts of ~1g were then placed into a crucible and either fired at their programmed regime one at a time or placed in vacuum storage. Other issues reported within the sample preparation include fluctuations in the furnace (up to 25°C) for up to 10 minutes at a time.

Ammonium Bifluoride Digestion

The most sample destructive component in this research is the use of ammonium bifluoride (ABF) for digestion. However, this is only a technique used to validate the experiments outlined in 4.7. This is a chemical digestion technique and to be used on material that has completed all other characterization techniques, as the process irreversibly destructs the sample.

Following Hubley, *et al.* [113] procedure, approximately 20 mg of NV1X series of NUGETS are loaded into a Savillex PFA 15 mL conical test tube. Solid ABF is added so that a 7:1 ABF to sample ratio was maintained and then the samples are heated for 30 minutes in an Al hot block at 230°C. A volume of 2 mL of HNO₃ is then added to each test tube which is then heated for 1 hour at 160°C in the Al hot block.

The aqueous samples are transferred to a PTFE beaker and rinsed with 18.3 MΩ high purity water then taken to near-dryness on a hot plate. The residue is dissolved in 2 mL of 8 M HNO₃ and transferred to a 15 mL Falcon test tube. The solution is then diluted to 10 mL with 18.3 MΩ high purity water. Rigorous studies in C-AAC proved that the concentration of the nitric acid during the sample heating does not have a large effect on the elemental recoveries of the NIST 610 glass [114]. Performing this digestion allows for a fast preparation and prevents the necessity of highly hazardous chemicals such as hydrofluoric acid. The possible recovery issues of this technique include Ca and Mg having a tendency to precipitate with F. Si was also expected to have poor recovery due to the reaction with ABF generating SiF₄ which volatilizes off as a gas.

Analysis Techniques

Inductively Coupled Plasma – Optical Emission Spectroscopy (ICP-OES)

Upon complete digestion, the NV1X series of NUGETS are measured through and ICP-OES to obtain high fidelity measurements of specific elements and their concentrations (Fig. 18). The solution from 4.6 is pumped through a peristaltic pump into a nebulizer to generate aerosol in the spray chamber, where approximately 10% of the analyte is actually transferred - the rest is drained due to the particle size being too large. Once in the spray chamber, the analyte is flushed through with argon gas, which both carries the analyte and is itself vaporized into a plasma by the ICP torch. The ion source for an ICP-OES, is a high temperature argon plasma coupled with a nebulized inlet spray. The discharge temperature for this is between 6,000 -10,000 K, producing mostly positive ions [117]. When the plasma cools, the electrons drop back down to ground level energy and emit light of the characteristic wavelength that is compared with a calibration plot to give the concentration for that element in the sample [117].

Handheld Laser Induced Breakdown Spectroscopy (HH-LIBS)

Laser Induced Breakdown Spectroscopy creates a laser induced plasma as the ion source for measurement. More specifically, it uses a pulsed laser to ablate the surface of a material into a plasma of ions, molecules, atoms, and particles [118]. LIBS is a primary technique for direct chemical analysis of solid samples and has a large following in the community of single particle analysis, and uranium isotope analysis [119,120]. One huge benefit to LIBS is that it can be performed in ambient conditions, meaning it does not require the use of utilities such as a vacuum pump. This also allows the device to be miniaturized and easily transported for use in field applications. Hand-held LIBS gained popularity due to its portability, quickness of results, and simplicity. There is the possibility of increased background noise dependent on the deployed environment.

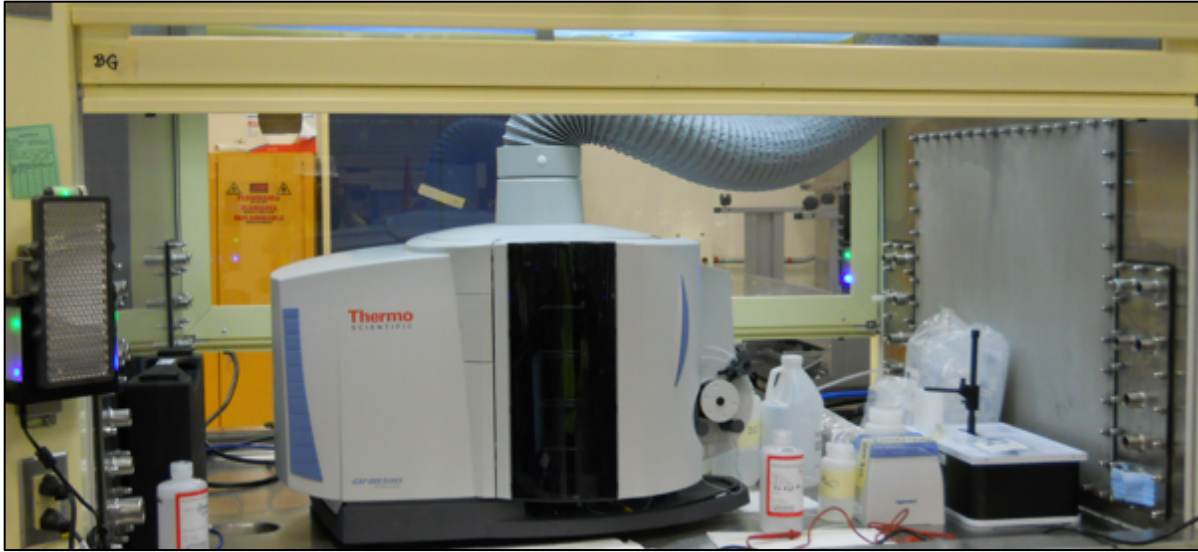


Figure 18: Image of Inductively Coupled Plasma-Optical Emission Spectrometer used in this study.

Therefore, it is important to note that this technique should be used in situations where onsite analysis is critical, and that removing the sample would either cause damage to the sample or create a hazardous environment for the analyst. The SciAps Z300 LIBS instrument was run in Element Pro mode, an uncalibrated mode, which formulates the relative abundances of elements within the sample as compared to one another. This is a non-traditional approach in LIBS measurements as normally, the use of standards with the appropriate matrix is critical to interpretation of spectra. However, the investigator is not going to have a reference material to calibrate to if the sample and its constituents are unknown. The fundamentals of interpreting this type of spectra is relatively new, and because the mode is not meant to be quantitative, developing a method to retrieve useful information from the peaks is crucial if this technique is to be considered for nuclear forensic applications.

The algorithm identifies the major peaks in a spectrum, matches them to the list in the LIBSLINES, and reports the major elements present if a certain fraction of peaks is present (>50% of all peaks listed) (Fig. 19). The relative abundance (RA) value is proportional to the size of that element's peak versus all other peaks seen in the spectrum, and the RA values are normalized to 100. This type of measurement is a crude, qualitative measure of what major elements are present, and roughly how large their peaks are. The line percent is a ratio comparing the number of lines that are detected in the spectra to the number of lines in the found in the library for an element and the likelihood rating uses this line percent to rate how likely it is that the element is actually present in the sample. While the option to tailor the internal libs line list is available to obtain higher confidence of relative abundances, it is not at the level of accuracy needed for nuclear forensic analysis. Therefore, it is crucial to further process the data through external means such as multivariate data analysis (MVDA).

For Example:

NVIC	Element	Relative Abundance	Lines	Likelihood
	Ca	36.5	100	151
	Al	18.1	71.4	187
	Ti	8.39	84.6	72.6
	Na	7.76	100	93.6
	Si	7.35	100	64.7
	Tl	4.29	50	0.456
	Mg	3.8	90.9	47.7
	Ag	2.88	60	7.38
	Fe	2.58	92.3	45.4
	K	2.45	50	43.1
	Mn	2.25	65.2	22.2
	Rb	1.37	50	3.01
	C	0.568	100	1.97
	Sr	0.485	50	4.26
	Pd	0.373	42.9	3.27
	Li	0.352	100	0.707
	Cs	0.271	50	2.38
	H	0.157	50	1.38

NaOH composition in NUGETS 1.52%
 SiO₂ composition in NUGETS 71.27%
 Element not in NUGETS

Figure 19: Example output from HHLIBS SciAps internal program. Highlighted and circled elements are indicated by image legend.

Multivariate Data Analysis: Partial Least Squares Regression (MVA: PLSR)

Partial Least Squares (PLS) Regression involves vectorization of input and output data, as well as a common inner transformation linking the two. This technique is helpful for data sets in which a predictive model is needed. It projects an objective transformation of the data to determine covariance and ultimately create a linear model that effectively relates the input and output data. A model is usually built to optimize predictive efficiency by selecting the number of latent variables required to compute an accurate new observation. The method of comparing across models assessed the RSME or the root mean squared error. This is a universal way to compare each model to determine the approach that performs the highest and used as the figure of merit in the discussion. It considers the predicted values of the model as compared to the actual values and assigns an error correlating to how accurate the given model performs.

PLS considers the input and output variables as well as an inner transformation in the complete algorithm used. The inputs, outputs, and inner transform are vectored in order to find the latent variables. These latent variables are found from an iterative process of using the largest eigenvector of between the given input and output and using the scores to project back on the original matrix resulting in the loadings. Each successive iteration has less predictive power because the highest eigenvector is used in the first iteration, so an optimal number of eigenvectors was selected through cross-validation. This method multiplies the test inputs by the inner transform vectors, which are correlated to both input and output data, and varies the ending latent variable to obtain the optimal number of latent variables which result in the minimum RMSE. Typically, pre-treatments on the data are done in an attempt to maximize differences due to sample differences and minimize differences from other sources such as normalization, mean-centering, and/or other appropriate standardization techniques. This is done to create an equal variance between all input data. While

all of the wavelengths possess the same units, it is still important to process the data this way for cross comparison of other measurements and future studies.

PLS has been used not only on a variety of LIBS spectra in science, but rather commonly on problems in the nuclear industry such as the detection of thorium in spent fuel [121, 122]. These empirical modeling techniques are tools for recognizing patterns and relationships between the input and output matrices, X and Y. They do not consider variables such as quality of sample, temperature effects, plasma physics, or any other attention to sampling parameters [123]. Thus, it is important to have a thorough discussion of the raw data and all spectra prior to conducting these analyses to account for discrepancies that may arise from the experimental set up, or possibly from material synthesis. The need to reduce the large arrays presented through unfiltered spectra have been noted in the literature and the initial approaches to this issue all center around omitting wavelengths where intensities are weak or nonexistent [122,123]. This method was explored but ultimately not utilized as excluding data can sometimes corrupt the predictive capabilities of PLS models. For example, the spectral range can be narrowed to include only areas pertaining to the known composition of the NUGETS, but if an unknown sample was shot with constituents outside of the elected range, classification of such sample would not be accurate. Additionally, all known spectral interferences can be removed from the model input data since there is not a definitive way to reduce these interferences during but doing so could lead to removal of rare emission lines.

Considerable effort was directed towards establishing a catalog of sub-models similar to that outlined in [116] Anderson *et al.* This method allows for a variety of small range PLS models to be trained and incorporated into a comprehensive program that linearly interpolates the composition of the unknown NUGETS. This is a method that has been successfully implemented

for ChemCam measurements on Mars geological samples and was anticipated to be successful in this approach.

CHAPTER 3: MULTIVARIATE ANALYSIS METHODS APPLIED TO HANDHELD LASER INDUCED BREAKDOWN SPECTROSCOPY (HHLIBS) SPECTRA OF POST- DETONATION SYNTHETIC NUCLEAR MELT GLASS (LA-UR- 20-25215)

Abstract

Rapid analysis of nuclear fallout poses a great challenge for the nuclear forensics' community. In this study, four nuclear underground engineered test surrogates (NUGETS) representative of nuclear debris in a post-detonation environment were analyzed with handheld laser induced breakdown spectroscopy (HHLIBS). The NUGETS were synthesized from a rath oxide matrix mirrored after the Nevada Test Site soil. An integration period of 1 millisecond and gate delay of 650 ns were used to collect 7 pulses per location at 3 locations with 10 cleaning shots per measurement. Partial Least Squares Regression was applied to the NUGETS spectrum in a variety of models, trained on 26 geological standards of varying compositions. All models predicted NUGET composition within 1 wt% of the measured composition and resulted in predicted root mean squared error (RMSEP) values under 1 wt%. For utilization in a field application, a larger range of standards would be recommended to train the model, but these results provide evidence that coupling LIBS spectra to PLSR can accurately determine elemental concentrations of unknown samples.

Introduction

Nuclear melt glass, product of a nuclear detonation event, is a slurry of geological material from the surrounding environment fused with device components. Characterization of this material on-site is difficult and presents many safety issues for first responders [124,125]. Removal of nuclear melt glass from the blast location could cause damage to the sample, create a hazardous

environment for the analyst, or contribute costly delays in emergency response. For rapid analysis of nuclear debris, there has been a recent push to utilize handheld laser induced breakdown spectroscopy (HHLIBS) as it can be operated in ambient conditions, uncalibrated, and on virtually any sample without preparation [126].

Benchtop LIBS is a primary technique for direct chemical analysis of solid samples and has a large following in the community of particle analysis, and uranium isotope analysis [7,127]. It has been proven an important tool in identifying the composition of metals for a variety of nuclear applications [128-131]. HHLIBS does not require the use of certain utilities as its benchtop counterpart such as a vacuum pump or large power source. The miniaturized version is easily transported for use in field applications [132]. However, being a spectroscopic technique there still exists issues pertaining to spectral interferences caused by matrix effects – contaminants, background noise dependent on the deployed environment, that arise during the plasma creation and subsequent measurement [133].

In the following study, the SciAps Z300 was run in Element Pro mode, an uncalibrated mode, that formulates the relative abundances of elements within the sample as compared to one another. In real life applications, the investigator is not going to have a reference material to calibrate to if the sample and its constituents is unknown. In order to obtain meaningful and quantifiable results, the spectra need to be processed through multivariate data analysis (MVDA). The goal of this study is to implement and optimize Partial Least Squares Regression (PLSR) on HHLIBS spectra of nuclear melt glass in order to obtain accurate percentages of elemental composition.

The act of measuring geological standards and glass samples are not scientifically complex beyond calculating appropriate gating and laser parameters to reduce matrix effects. This is dependent on high level plasma physics interactions and it is not in the scope of this paper to elaborate in detail,

but further information can be found in [134]. The scientific value of this paper lies in deriving quantitative information from the raw spectrum from measurements on samples with unknown composition. This issue is addressed through the introduction of the MVDA technique, PLSR which has been demonstrated on a variety of materials including thorium based-fuel debris [135], rare earth elements in phosphors [136], as well as unknown Martian soil [115].

The models formulated in this study were created via a python program known as Point Spectra GUI [116] which can be used for multiple regression analyses. For this study, Partial Least Squares (PLS) Regression was selected due to its simplicity and effectiveness handling multi-dimensional data sets. PLS involves vectorization of input and output data, as well as a common inner transformation linking the two. This technique is suitable for data sets in which a predictive model is needed. It projects an objective transformation of the data to determine covariance and ultimately create a linear model that relates the input and output data [137]. Latent variables are assigned from an iterative process of using the largest eigenvector of between the given input and output and using the scores to project back on the original matrix resulting in the loadings [138]. Each successive iteration has less predictive power because the highest eigenvector is used in the first iteration, so an optimal number of eigenvectors is often selected through cross-validation (CV). This method multiplies the test inputs by the inner transform vectors, which are correlated to both input and output data, and varies the ending latent variable to obtain the optimal number of latent variables which result in the minimum root mean squared error (RMSECV). PLS is a notably simple predictive tool, yet consistently yields better results when compared to other popular regression methods [139].

Experimental Setup

The nuclear melt glass used in this study is a surrogate (containing no actinides) formulated from the soil composition of southern Nevada and crafted to simulate debris produced from underground nuclear detonations. The NV1X series of nuclear underground engineered test surrogates (NUGETS) were selected for validation of the PLSR model. These NUGETS were made by Gilbreath *et al* [110] from a rath oxide matrix and fired to the temperatures and time scales listed in Table 5. However, because these samples are not certified or standard reference material, their composition was measured through ABF (ammonium bi-fluoride) digestion and ICP-OES (inductively coupled plasma – optical emission spectroscopy) for quality assurance.

The most sample destructive component in this study is the use of ABF for digestion. This is a chemical digestion technique and to be used on material that has completed all other characterization techniques, as the process irreversibly destructs the sample. Following Hubley, *et al.*[113] procedure, approximately 20 mg of NV1X series of NUGETS are loaded into a Savillex PFA 15 mL conical test tube. Solid ABF is added so that a 7:1 ABF to sample ratio was maintained and then the samples are heated for 30 minutes in an Al hot block at 230 °C. A volume of 2 mL of HNO₃ is then added to each test tube which is then heated for 1 hour at 160 °C in the Al hot block. The aqueous samples are transferred to a PTFE (poly-tetrafluoride ethylene) beaker and rinsed with >18 MΩ high purity water then taken to near-dryness on a hot plate. The residue is dissolved in 2 mL of 8 M HNO₃ and transferred to a 14 mL Falcon test tube. The solution is then diluted to 10 mL with >18 MΩ high purity water. Rigorous studies by Hubley, *et al.* proved that the concentration of the nitric acid during the sample heating does not have a large effect on the elemental recoveries of the NIST 610 glass [114].

Performing this digestion allows for a fast preparation and prevents the use of highly hazardous chemicals hydrofluoric acid. The possible recovery issues of this technique include Ca and Mg having a tendency to precipitate with F. Silicon obviously was expected to be removed from the sample matrix due to the reaction with ABF generating SiF₄ and volatilizes off in a gaseous form. Upon complete digestion, the NV1X series of NUGETS were measured through and ICP-OES to obtain high fidelity measurements of specific elements and their concentrations.

HHLIBS measurements

The geological standards (Table 7 in **Post-Detonation Material**) for LIBS measurements were prepared by filling 30 mm Spex aluminum cups with 3-5 grams of material. The powders were then pressed to 35 kpsi for 5 minutes. A commercially available handheld SciAps Z300 LIBS was used to measure 26 geological standards, as well as the 4 NUGETS in the NV1X series. This instrument is a class 3B laser with a laser wavelength of 1064 nm. For the geological standards, the laser and data collection parameters were set with an integration period of 1 millisecond and 650 ns delay on 4 locations with 0 cleaning shots and 16 pulses per location translating to a total of 64 spectra collected per sample. This was completed 5 times on each sample surface at a frequency of 50 Hz. A variety of measurement parameters were used to collect data on the NUGETS NV1X series. This was to test whether the laser and data collection parameters had a large influence on predictive capabilities of the PLS model. The parameters that remained constant were the integration period and delay, consistent with that of the standards at 1 millisecond and 650 ns, respectively. The cleaning shots, locations, and pulses per location for the NUGETS measurements were 10, 3, and 7 respectively. The effects of varied acquisition settings are discussed in subsequent sections.

Point Spectra GUI Procedure

The standards data was uploaded to include composition of each compound and intensity of each wavelength measured with HH-LIBS from 188 nm to 600 nm due to machine limitations. Local Outlier Factor was applied to the data to eliminate extraneous data that could corrode the model performance. The number of outliers removed varied depending upon which element was being analyzed. Because the data did not contain different units, there was no standardization measure applied. Stratified folds were run on the standards data in order to split folds for cross validation (CV), which inherently assigns one-fold for testing. Nine folds were assigned for each element, designating the third fold for testing. CV was applied to the data and plotted against various parameters. A variety of regression algorithms were tested and compared before selecting the final number of LVs to optimize the model. CV was repeated for a variety of compositional ranges within the standard data set (Table 8). PLS regression training was then applied on the training set for the different sub-model ranges. The training data and test data were both predicted, and the former sub-models were then blended, optimizing for the known compositions of interest to predict. Finally, the same blended ranges were utilized on the test set predictions without optimization. The models were all compared by their RMSE values in order to assess performance and accuracy in the case of the test set. Several iterations were done before the NUGETS data set was analyzed through the finalized model.

Results and Discussion

In Table 9 below, the percent relative abundance of each element is shown as measured through ICP-OES post ABF dissolution (ABF%) for each NUGETS type. It is compared to the original powder matrix of the glasses, pre-firing (Composition %), which is the same for all NUGETS.

Table 8: Sub-model ranges of the training data

Si	Range	LVs	Mn	Range	LVs
Full Model	17.86-36.13	4	Full Model	0.01-0.31	9
High	26-36.13	7	High	0.15-0.31	9
Low	17.86-27	5	Low	0.01-0.17	9
Ti			Na		
Full Model	0.01-1.64	7	Full Model	0.33-3.34	7
High	0.9-1.64	7	High	1-3.34	7
Low	0.01-0.95	7	Low	0.33-2	5
Al			Fe		
Full Model	4.92-10.37	6	Full Model	1.22-10.03	6
High	7-10.37	7	High	4-10.03	7
Low	4.92-8	7	Low	1.22-6	6
Ca			Mg		
Full Model	0.31-7.07	5	Full Model	0.02-5.42	7
High	2.0-7.07	6	High	1-5.42	5
Low	0.31-2.50	6	Low	0,02-1.5	3
K					
Full Model	0.03-4.51	6			
High	3-4.51	3			
Low	0.03-4	6			

While the ABF percentages (Table 8) between NUGETS vary, they follow an overall trend matching the original composition, apart from Mn and Ti. It was expected that Ca and Mg would have poor recoveries due to precipitation with fluoride. Additionally, Si reacts with ABF, generating SiF₄ that volatilizes off as a gas. However, the percentages of these elements measured in this experiment mostly met the original composition percent. However, it is noted in Gilbreath's thesis that underground melt glass tends to vary in many physical factors including crystallinity and amount and type of inclusions [110]. This work verifies the synthesis method of the NUGETS by Gilbreath and validates further the use of ABF digestion in plasma injection-based measurements (ICP-OES, ICP-MS). This is a novel development in itself, as the determination of melt glass compositions is extremely desired for post-detonation debris in a nuclear forensic scenario. The number of outliers removed from each model is noted in Table 10 along with the number of spectra in the training and test sets, as well as the number of standards (type) contained in the training set. A combination of Local Outlier Factor (LOF) and human quantitative analysis was used in removing samples with outlying spectral emissions (LOF) and compositional ranges (human). From the training set, the minimum RMSECV was not accomplished at the same number of LVs for each element. The appropriate number of latent variables (LVs) was selected based on where the elbow of the curve begins when plotting RMSECV versus the number of LVs. There seemed to be no apparent effect from varied LIBS acquisition settings such as number of cleaning shots. The models seemed to rely more on the number of emission lines present rather than the intensity, which is more commonly influenced by acquisition settings. The Full model and blended submodel approaches typically performed better than that of the High or Low models when analyzing the same element. The selection of submodel ranges varied between elements and can be seen in Figure 20.

Table 9: Weight percent concentration of elements in NUGETS and NIST610.

Element	NV1A	NV1B	NV1C	NV1D	NIST610
Al	5.52	7.42	8.54	8.34	1.06
Ca	1.22	1.79	2.34	2.09	8.58
Fe	0.89	1.04	1.35	1.52	0.05
K	1.92	3.52	3.51	2.59	0.05
Mg	0.27	0.40	0.53	0.46	0.00
Mn	0.45	0.60	0.66	0.59	0.05
Na	0.32	0.61	0.80	0.70	10.39
Si	26.82	38.39	33.94	35.99	33.66
Ti	1.40	1.51	1.98	2.24	0.04

Table 10: PLSR model formation parameters for each element

	Si	Ti	Al	Ca	K	Mn	Na	Fe	Mg
Outliers removed (spectra)	13	13	15	20	10	5	15	20	15
Spectra in Test Set	15	15	15	20	15	15	15	15	15
Spectra in Training Set	102	102	100	90	105	110	100	95	100
Samples in Training Set	21	21	20	18	21	22	20	19	20

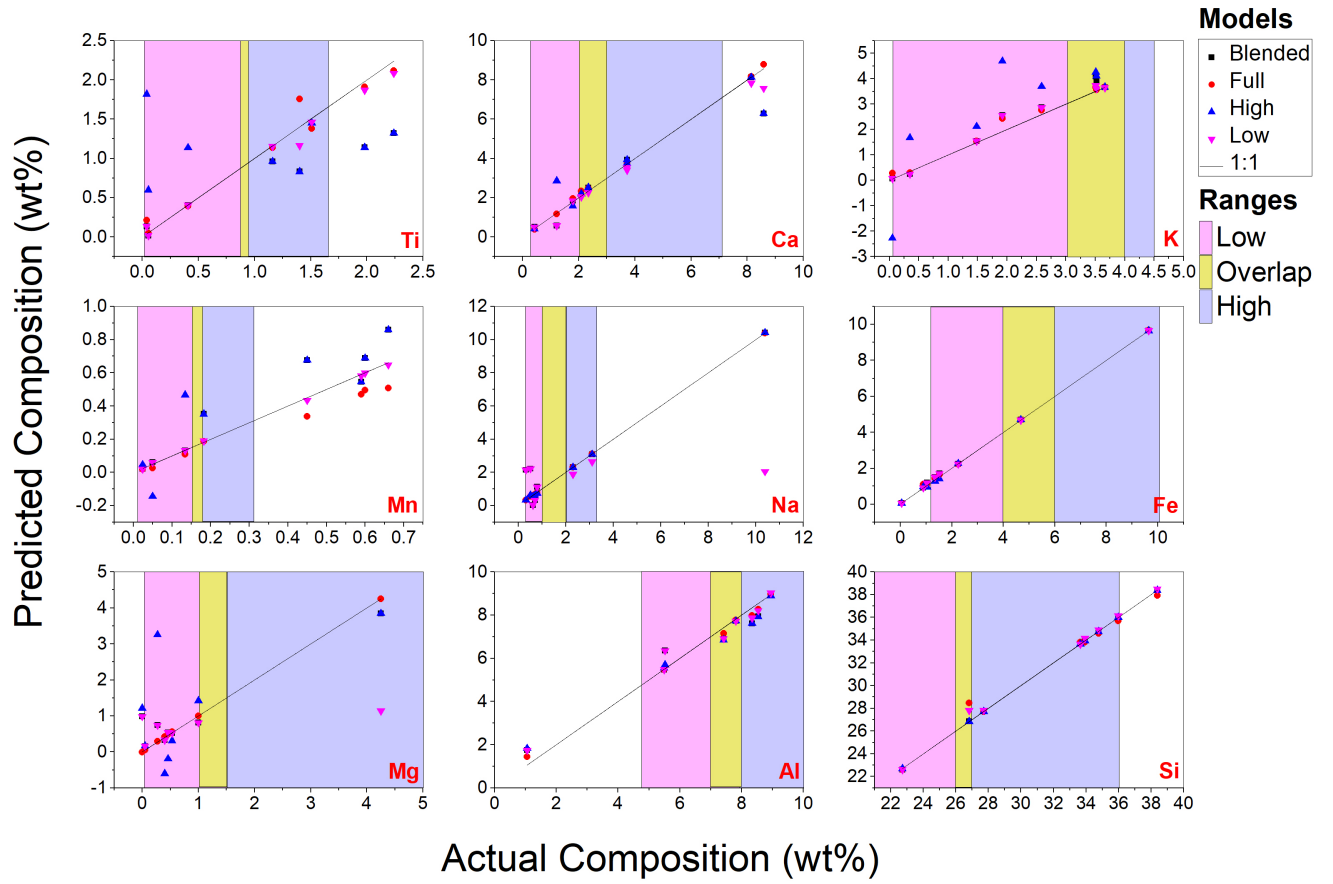


Figure 20: Model predictions for composition of NUGETS, NIST610, and Test Standards combined for each element plotted against actual composition values.

Blended ranges were selected by identifying a median, and overlapping the models based on the skew of the compositions in the standards file (Fig. 20). For example, in the Ca model, there were very few standards with a composition above 3 wt%. The low model was selected to contain most of this information, while the high model dealt with higher, less present compositions. Prediction appeared to improve when there were a greater number of standard samples in the trained models whose composition more closely follows that of the NUGETS in range. When the standard sample compositions vary, the Full Model approach is sufficient in predicting compositions of unknown value for example, with Ti. The range for Ti is from 0.01-1.64 whereas the NUGETS range from 1.4-2.24, therefore, not only is there a large amount of data included that doesn't fall under our unique sample compositions, and the model is left to extrapolate outside of its intended range.

To assess the models formulated to predict these compositions, RMSEP values are of critical importance. These values represent how effective the model is at predicting new outputs (RMSEP). The number of LVs used in each model affects the RMSE values dramatically. These vary depending on what element is being assessed which demonstrates the importance of maintaining separate models. The number of LVs selected for each element varied from 4 to 7. When assessing the curve of RMSECV to LV, selecting too large a number of LVs can lead to overfitting to a particular data set and rendering it useless in the prediction of unique data. Namely, developing a successful model does not translate to utilizing the lowest RMSE. Generally, an LV was selected representing the second to lowest RMSECV value.

Issues that arose were i) not having enough samples in the training set that represented the full range of compositions present in the NUGETS (i.e. Ti models) ii) having too wide of a range of compositions in the training set for elements where the NUGETS have a particularly small range (i.e. K models). The former of these left the model to extrapolate an output which it is not PLSRs

intended use. The latter of these issues was prevalent and seemed to defeat the use of blended models, particularly in samples with low weight percent compositions (<1%). As shown in Table 11, the RMSEP values remained less than 1 for every element for both the blended and full models performed on NUGETS and Test Standards. However, the full models performed either equal or better to the blended models in more than 88% of elements measured for the NUGETS samples. This is in part to influence on the models by selection of LVs. When a lower number of LVs are chosen for the full model than for the high and low models of the same element, typically the blended model will perform better such as in the case of Si. The full models also performed better due to the use of a small range set of compositions.

It is imperative that a standard be trained and tested in each compositional range for the blended model to give an improved RMSEP as compared to the full model. When approaching this issue from the viewpoint that you do not know the composition of your unique samples, it is difficult to assign blended ranges that are truly representative. To counter this, it would be recommended in future studies to expand the training and test sets to include a wider range of compositions. Despite these disadvantages, less than 3.5% of the predicted compositions exceeded +/-1 wt% from the actual composition for the blended and full models in the NUGETS, NIST610, and Test Standards combined (total of 146 outputs). NV1A showed the most discrepancy in models among the NUGETS samples, accounting for 40% of the predictions exceeding +/-1% wt% from the actual composition with NIST610 accounting for another 40% (Fig. 21). NV1A sample could be severely inhomogeneous as the LIBS data contains a variety of conflicting spectral lines among separate measurements. In a field application, the integrity and state of the sample is relatively uncontrollable. The recommended approach would be to average a larger number of spectra to yield a more accurate result.

Table 11: RMSEP Values for Blended and Full Models

Element	Blended Submodels		Full Models	
	Standards	NUGETS	Standards	NUGETS
Si	0.05	0.01	0.11	0.88
Ti	0.12	0.68	0.02	0.68
Al	0.06	0.68	0.04	0.27
Ca	0.11	0.34	0.03	0.16
K	0.07	0.49	0.05	0.28
Mn	0.1	0.16	0.02	0.12
Na	0.98	0.99	0.01	0.02
Fe	0.01	0.13	0.02	0.13
Mg	0.26	0.24	0	0.03

The NIST610 models predicted falsely due to its inclusion in the Mg models despite having 0 wt% Mg. This was a test to see if these models would predict a false composition in the absence of the tested element. While the blended model registered a wt% of 0.98 Mg, the Full model surprisingly recorded a wt% of -0.01 Mg. In addition to the bias imposed when formulating these models (selection of LVs, blended ranges, exclusion of outliers), there are spectral factors to consider. In LIBS measurements, the intensities fluctuate depending on the elemental abundance and can experience interference with other elements within the sample.

The intensity of wavelength also does not scale with composition, causing the model to rely more on the presence of emission lines rather than their intensities. For example, Ca and Al have 2 primary lines at 396.847 nm and 396.152 nm respectively. In the NUGETS and NIST610 samples, the intensities of these two peaks ranged from 21000-30000, while the primary peak for Si hardly reached 13000.

When compared to the composition of these elements in each sample, it becomes apparent why a more sophisticated relationship must be established to accurately contrive concentration from spectra. This initially inspired the use of the blended sub-model approach, where not only is the model using averaged data, but it is comparing separate models, and blending the outcome to overall improve the accuracy of the predictions for each element.

However, the majority of elemental models were predicted successfully with the full model and in fact, increased in error with the use of a blended submodel. It is expected that if utilizing a larger range of compositions in the training set, as well as a larger number of standards, there would be more significant improvement of the blended submodel predictions. Anderson *et al.* demonstrated this using over 400 known standards to predict the composition of Martian soil from ChemCam on the Curiosity Rover with a blended submodel approach [116].

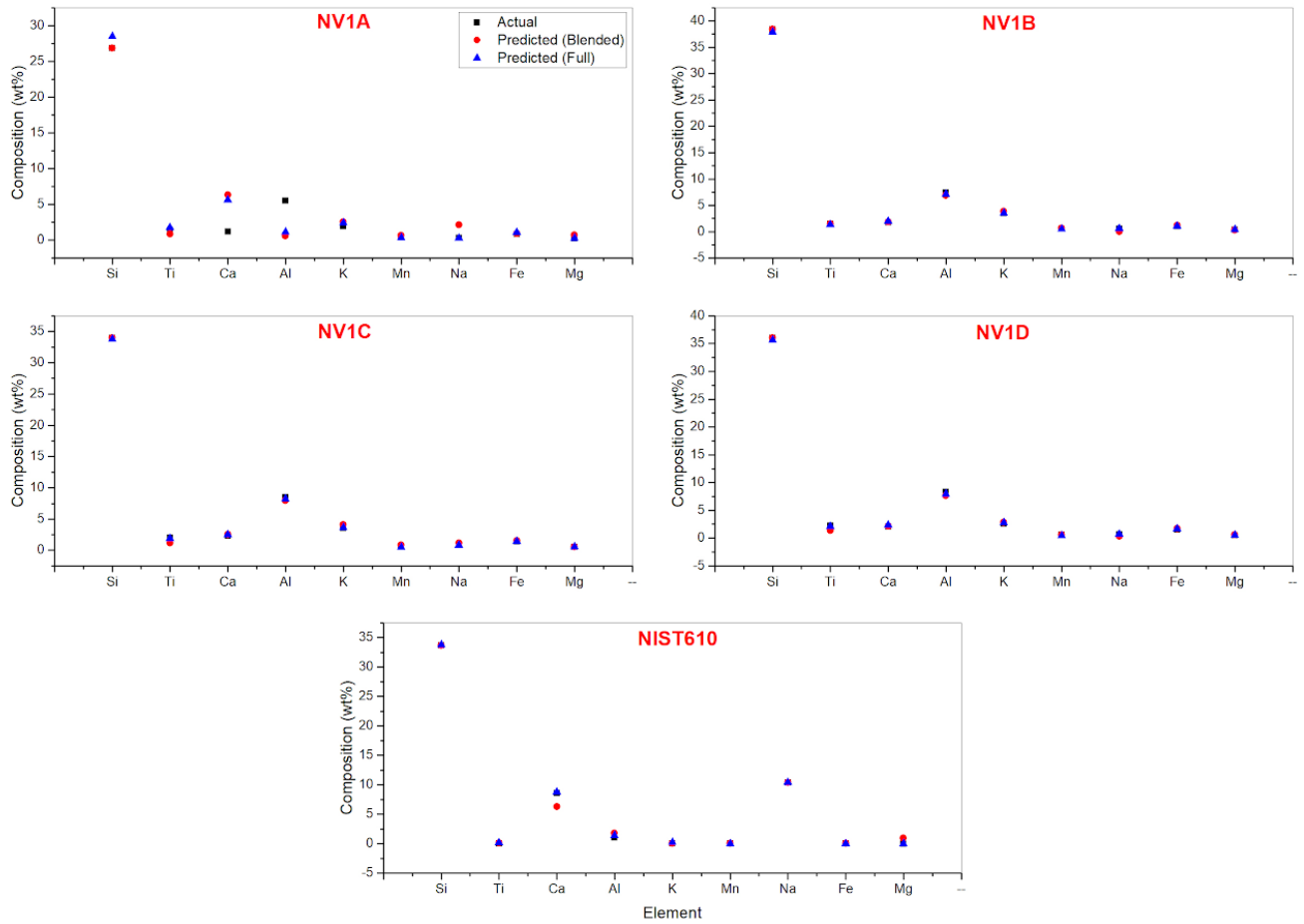


Figure 21: NUGETS and NIST610 prediction results the blended and full models for each element.

Conclusions and Recommendations

The percent relative abundance of each element was successfully measured through ICP-OES post ABF dissolution (ABF%) for each NUGETS type. Applying PLSR to the LIBS data accurately predicted each NUGETS elemental composition within +/-1 weight percent 100% of the time for each full model and 97% of the time for each blended submodel. While the blended submodel approach did not yield consistent results of lower error (RMSEP) than the full models, it is still expected that the latter is useful when dealing with a larger range of compositions. In this proof of concept study, the 26 standards were selected having knowledge of the NUGETS composition, yet still struggled to account for the full range of elemental compositions. When developing a model for targeted forensics use, it is recommended to select a training set of standards with compositions large enough to fully span the expected sample composition as it could improve the use of submodels. While the exact composition of nuclear melt glass would be unknown, educated estimations of ranges can be interpreted from a variety of location-sensitive studies [110]. Safe practice would be to measure an equal distribution of standards from 0%-100%.

CONCLUSIONS

Forensics analysis of SNM such as Pu-239 is complicated by a variety of processes including oxidation, damage accumulation, and device detonation. These processes chemically alter the material over time and are highly dependent on temperature and environment. This work presented studies on Cu metal as an analogue material for SNM. Analysis of the metallic oxide layer through O-isotope analysis indicated the atmosphere in which the material was aged can be deduced from O-isotope values of local water vapor, due to their marked geographical dependence. With increasing temperature, a greater uptake of ^{18}O was observed in the growing oxide layer. While this study focused on accelerated aging, further research under more realistic aging time scales with better controlled environments is needed in order to further improve the interpretation and calibration of this forensic isotopic signature. Future studies would include oxidation of Cu in varied proportions of O_2 versus water vapor contents, where the atmospheres would be measured for precise O isotope values. Isotopic measurements are now possible through laser spectroscopic methods and satellite- and ground-based infrared absorption techniques, which enables this technique to be easily adaptable to routine safeguards inspections in a variety of locations. Damage accumulation on the surface of Cu metal was shown to translate to the growing oxide layer in a suppression of the outer most oxide phase (CuO). This was attributed to damage on both the metallic surface and the initial Cu_2O nodule growth *in-situ*. The combination of defects produced on the Cu metal surface and the Cu_2O monolayer accurately represents the Pu-239 system of simultaneous alpha-decay and oxidation. Future studies should be aimed toward reproducing these SEM results and drawing comparison to a pristine sample introduced into the beam line target chamber at 200°C without irradiation. Upon exposure to high temperature mixing in a detonation event, nuclear debris concentration was accurately predicted through handheld laser induced

breakdown spectroscopy (HHLIBS) coupled to partial least squares regression (PLSR). Full range models demonstrated the advantages of tailoring training input towards site-specific soil estimates, while blended submodels are better suited to analysis of completely unknown soil compositions. While the blended submodel approach did not yield consistent results of lower error (RMSEP) than the full models in this experiment, it is still expected that the latter is useful when dealing with a larger range of compositions (e.g. Mars Rover LIBS). Future studies could tailor compositional ranges based on geographic location. While the exact composition of nuclear melt glass would be unknown, educated estimations of ranges can be interpreted from a variety of location-sensitive studies. Further, it would be useful to expand this technique to NUGETS that contain fission products.

REFERENCES

1. Hecker, Siegfried S., *et al.* "Aging of Plutonium and Its Alloys," *Los Alamos Science*, 26, 238-243, (2000).
2. Baclet, Nathalie, *et al.*, "Self-irradiation effects in plutonium alloys stabilized in the δ -phase," *Journal of Nuclear Science and Technology*, 39, 3, 148-151, (2002).
3. Chung, Brandon, *et al.* "Effects of self-irradiation in plutonium alloys," *Journal of Nuclear Materials*, 471, (2015).
4. Stakebake, J.L. "The High Temperature Oxidation of Plutonium-3.3 a/o Gallium," *Journal of Electrochem. Soc.: Solid State Science and Technology*, 124, 3, 460-465, (1977).
5. Haschke, John M., *et al.* "Surface and Corrosion Chemistry of Plutonium," *Los Alamos Science*, 26, 252-273, (2000).
6. "Plutonium Crystal Phase Transitions," *Plutonium Crystal Phase Transitions*, GlobalSecurity.org, (2011).
7. Mayer, K. *et al.* "Nuclear forensic science: correlating measurable material parameters to the history of nuclear material," *Chem. Rev.*, 113, 884–900, (2013).
8. Varga, Zsolt, *et al.* "Methodology for the Preparation and Validation of Plutonium Age Dating Materials" *Analytical Chemistry*, 90, 4019-4024, (2018).
9. Kristo, Michael J., *et al.* "Nuclear Forensic Science: Analysis of Nuclear Material Out of Regulatory Control" *Annual Review of Earth and Planetary Sciences*, 44, 555-79, (2016).
10. Korzhavyi, P. A., *et al.* "Literature review on the properties of cuprous oxide Cu₂O and the process of copper oxidation," Swedish Nuclear Fuel and Waste Management Co. Internal Report, TR-11-08, (2011).
11. Ebisuzaki, Y., *et al.* "Oxidation Kinetics of Copper," *Journal of Chemical Education*, (62), 4, 341- 343, (1985).

12. Narayan, J., *et al.* "Ion radiation damage in copper," *Journal of Nuclear Materials*, 71, 1, 160-170, (1977).
13. Zinkle, S.J., *et al.* "Defect microstructure in copper alloys irradiated with 750 MeV protons," *Journal of Nuclear Materials*, 212-215, 1, 132-138, (1994).
14. Singh, B.N., *et al.* "Defect accumulation in pure fcc metals in the transient regime: a review," *Journal of Nuclear Materials*, 206, 2-3, 212-229, (1993).
15. Avdeeva, A V, *J. Phys.: Conf. Ser.* 653 012028, (2015).
16. Jörg Boxhammer, "Shorter test times for thermal- and radiation-induced ageing of polymer materials: 1: Acceleration by increased irradiance and temperature in artificial weathering tests," *Polymer Testing*, 20, 7, 719-724, (2001).
17. Wright, Richard N., "Summary of Studies of Aging and Environmental Effects on Inconel 617 and Haynes 230" Idaho National Laboratory, (2006).
18. Wang, Jing, *et al.*, "Combined effects of surface oxidation and interfacial intermetallic compound growth on solderability degradation of electrodeposited tin thin films on copper substrate due to isothermal ageing," *Corrosion Science*, 139, 383-394, (2018).
19. Gavgali, M., *et al.*, "The effects of artificial aging on wear properties of AA 6063 alloy," *Material Letters*, 57, 3713-3721, (2003).
20. Biccari, Francesco "Defects and Doping in Cu₂O," *PhD Thesis Sapienza Università di Roma* (2009).
21. Wang, Y. *et al.* "Electronic structures of Cu₂O, Cu₄O₃, and CuO: A joint experimental and theoretical study," *Physical Review B: Condensed matter and materials physics, American Physical Society*, 94, 24, 245418, (2016).

22. Debbichi, Lamjed, *et al.* "Electronic structure, lattice dynamics and thermodynamic stability of parameltaconite Cu₄O₃," *Materials Chemistry and Physics*, 148, 293-298, (2014).
23. Zhou, Guangwen "Dynamics of Copper Oxidation Investigated By *In Situ* Uhv-Tem," University of Pittsburgh, Doctor of Philosophy in Material Science and Engineering, (2003).
24. Jae Won, Lim, *et al.* "Brief review of oxidation kinetics of copper at 350°C to 1050°C," *Metallurgical and Materials Transactions A*, 37A, 1231-1237, (2006).
25. Gattinoni, Chiara, *et al.* "Atomistic details of oxide surfaces and surface oxidation: the example of copper and its oxides," *Surface Science Reports*, 3, 70, 424-447, (2015).
26. Wolfer, Wilhelm G., "Radiation Effects in Plutonium: What is known? Where should we go from here?" *Los Alamos Science*, 26, (2000).
27. Naundorf, V, *et al.*, "Production rate of freely migrating defects for ion irradiation," *Journal of Nuclear Materials*, 186, 227-236, (1992).
28. Stoller, R. E., *et al.* "On the use of SRIM for computing radiation damage exposure," *Nucl. Instruments Methods Phys. Res. Sect. B Beam Interact. with Mater. Atoms*, 310, 7580, (2013).
29. Lappin, Derry, *et al.* "An experimental study of electrochemical polishing for micro-electrodischarge-machined stainless-steel stents," *Jrnl. Of Mat. Sci.: Mat. In Med.*, 23, 2, 349- 356, (2012).
30. L.M. Garrison, G.L. Kulcinski, "The effects of tungsten's pre-irradiation surface condition on helium-irradiated morphology," *J. Nucl. Mater.*, 466, 302-311, (2015).
31. Zinkle, S.J., *et al.* "Microstructure of copper following high dose 14-MeV Cu ion irradiation," *Journal of Nuclear Materials*, 138, 1, 46-56, (1986).
32. ASTM E521

33. Benson, Sarah, *et al.* “Forensic applications of isotope ratio mass spectrometry – A review,” *Forensic Science International*, 157, 1-22, (2006).
34. Meier-Augenstein, W. “Applied gas chromatography coupled to isotope ratio mass spectrometry” *Journal of Chromatography A*, 842, 351-371, (1999).
35. Howa, John D., *et al.* “Isolation of components of plastic explosives for isotope ratio mass spectrometry” *Forensic Chemistry*, 1, 6-12, (2016).
36. Benson, Sarah, *et al.* “Forensic analysis of explosives using isotope ratio mass spectrometry (IRMS) – Discrimination of ammonium nitrate sources” *Science and Justice*, 49, 73-80, (2009).
37. Gentile, N., *et al.* “On the use of IRMS in forensic science: Proposals for a methodological approach” *Forensic Science International*, 212(1-3), 260-271, (2011).
38. Princeton Instruments “Raman Spectroscopy Basics” 1-5.
http://web.pdx.edu/~larosaa/Applied_Optics_464-564/Projects_Optics/Raman_Spectroscopy/Raman_Spectroscopy_Basics_PRINCETON-INSTRUMENTS.pdf
39. Villa-Aleman, Eliel, *et al.* “Characterization of uranium tetrafluoride (UF₄) with Raman spectroscopy,” *Journal of Raman Spectroscopy*, 47 (7), 865-870, (2016).
40. Rondahl, Stina Holmgren, *et al.* “Comparing results of X-ray diffraction, A mu-Raman spectroscopy and neutron diffraction when identifying chemical phases in seized nuclear material, during a comparative nuclear forensics exercise,” *Journal of Radioanalytical and Nuclear Chemistry*, 315, 2, 395-408, (2018).
41. Shiryaev, Andrey A. *et al.* “Forensic study of early stages of the Chernobyl accident: Story of three hot particles” *Journal of Nuclear Materials*, 511, 83-90, (2018).

42. Rickert, K. *et al.* "Assessing UO₂ sample quality with μ -Raman spectroscopy" *Journal of Nuclear Materials*, 514, 1-11, (2019).
43. Elorrieta, J.M., *et al.* "Temperature dependence of the Raman spectrum of UO₂" *Journal of Nuclear Materials*, 503, 191-194, (2018).
44. Lang, M., *et al.* "Characterization of ion-induced radiation effects in nuclear materials using synchrotron X-ray techniques," *Journal of Materials Research*, 30, 1366-1379 (2015).
45. Nuclear Forensics and Attribution Act [Public Law 111–140, 111th Congress.
46. Booth, C.H., *et al.* "Effect of temperature and radiation damage on the local atomic structure of metallic plutonium and related compounds," *Advances in Physics: X*, 2, 1, 1-21, (2017).
47. Tsarenko, I.A., *et al.* "Oxidation of Plutonium Metal," *Atomic Energy*, 89, 954-960, (2000).
48. Lohrengel, M.M., *et al.* "Growth, corrosion and capacity of copper oxide films investigated by pulse techniques," *Electrochimica Acta*, 32, 5, 733-742, (1987).
49. Chan ,Ho Yeung H., *et al.* "Oxide Film Formation and Oxygen Adsorption on Copper in Aqueous Media as Probed by Surface-Enhanced Raman Spectroscopy," *J. Phys Chem. B*, 103, 2, 357-365, (1999).
50. Niedrig-Schedel, Thomas, *et al.* "Copper (sub)oxide formation: a surface sensitive characterization of model catalysts," *Phys. Chem. Chem. Phys.*, 2, 2407-2417, (2000).
51. Kendall, Carol, *et al.* "Fundamentals of Isotope Geochemistry: Isotope Tracers in Catchment Hydrology," *Elsevier Science B.V., Amsterdam*, (2), 51-86, (1998).
52. Yapp, Crayton J. "Oxygen isotopes in iron (III) oxides," *Chemical Geology*, 85, 3, 329-335, (1990).

53. M.J.Graham, *et al.* "The Growth and Stability of Passive Films," *Corrosion Science*, 35, 1-4, 13-18, (1993).
54. R.J. Hussey and M.J. Graham, *Oxid. Metals* 45, 349 (1996).
55. M.P.Brady, *et al.* "Tracer Film Growth Study of Hydrogen and Oxygen from the Corrosion of Magnesium in Water," *J. Electrochem. Soc.*, 2014161, 9, C395-C404; doi:10.1149/2.0821409jes
56. Plekhanov, V.G. "Isotope effects on the lattice dynamics of crystals," *Materials Science and Engineering: R: Reports*, 35, 4-6, 139-237 (2001).
57. Koreiba, M. A., *et al.* "Isotope effects in the lattice structure and vibrational and optical spectra of Li/Li-YF:Ho crystals," *Institute of Spectroscopy*, Russian Academy of Sciences (1993).
58. Hagemann, H. *et al.* "Raman Spectra of Single Crystal CuO," *Solid State Communications*, 73, 6, 447-451, (1990).
59. Levitskii V. S., *et al.* "Raman Spectroscopy of Copper Oxide Film Deposited by Reactive Magnetron Sputtering," *Technical Physics Letters*, 41, 11, 1094–1096, (2015).
60. Zheng, Yao-Ting *et al.* "In-situ Raman monitoring of stress evaluation and reaction in Cu₂O oxide layer," *Materials Letters*, 78, 11-13, ISSN 0167-577X, (2012).
61. Holmlund, Joakim, *et al.* "Two-magnon Raman scattering from the Cu₃O₄ layers in (Sr₂, Ba₂)Cu₃O₄Cl₂," *Physical Review B*, 79, 085109, (2009).
62. Zoolfakar, Ahmad Sabirin, *et al.* "Nanostructured copper oxide semiconductors: a perspective on materials, synthesis methods and applications," *Journal of Materials Chemistry C*, Feature Article (2014).
63. Gulbransen, E.A., *et al.* "Oxidation of Copper between 250 ~ and 450~ and the Growth of CuO 'Whiskers'," *Journal of the Electrochemical Society*, (108), 2, 119-123, (1961).

64. Wei, Tao “Raman Scattering of Cupric Oxide (CuO),” *Master Thesis*, Simon Fraser University (1990).
65. Shao-Kuan Lee, *et al.* “Oxidation Behavior of Copper at a Temperature below 300°C and the Methodology for Passivation,” *Materials Research* 19(1): 51-56 (2016).
66. Meyer, B.K. “Binary copper oxide semiconductors: From materials towards devices,” *Phys. Status Solidi B*, 249, 8, 1487-1509, (2012).
67. Wang, Y. *et al.* “Electronic structures of Cu₂O, Cu₄O₃, and CuO: A joint experimental and theoretical study,” *Physical Review B: Condensed matter and materials physics, American Physical Society*, 94, 24, 245418, (2016).
68. Bernstein, Richard B. “Oxygen-18 Isotope Effect in the Reaction of Oxygen with Copper,” *The Journal of Chemical Physics*, 23, 10, (1955).
69. Brown, John B., *et al.* “Fractionation of Oxygen Isotopes in the Formation of Oxide Films on Copper,” *The Journal of Chemical Physics*, 27, 251, (1957).
70. Kroopnick, P. & Craig, H. “Atmospheric oxygen: isotopic composition and solubility fractionation,” *Science*, 175, 4017, 54-55, (1972).
71. Zheng, Yong-Fei “Calculation of oxygen isotope fractionation in metal oxides,” *Geochimica et cosmochimica Acta*, 55, 3399-2307, (1991).
72. Friedman and O'Neil (1977).
73. Sauders, W.H. *et al.* “Reaction Rates of Isotopic Molecules,” *Wiley*, New York, (1981).
74. Lee, Xuhui, *et al.* “Water Vapour ¹⁸O/¹⁶O Isotope Ratio In Surface Air In New England, USA,” *Tellus B: Chemical and Physical Meteorology*, 58, 4, 293-304, (2006).
75. Galewsky, Joseph, *et al.* “Stable Isotopes in Atmospheric Water Vapor and Applications to the Hydrologic Cycle,” *Rev. Geophys.*, 54, 809-865, (2016).

76. Atomic Energy Act of 1954 (P.L. 83–703).
77. (2018). Nuclear posture review report. Washington, DC: U.S. Dept. of Defense.
78. Mathew, Kattathu, *et al.* “Intercomparison of the Radio-Chronometric Ages of Plutonium-Certified Reference Materials with Distinct Isotopic Compositions,” *Analytical Chemistry*, 91, 18, 11643-11652, (2019).
79. Fitzgerald, Ryan, *et al.* “How Old Is It? - $^{241}\text{Pu}/^{241}\text{Am}$ Nuclear Forensic Chronology Reference Materials” *J Radioanal Nucl Chem*, 307, 3, 2521-2528, (2016).
80. Pommé, S., *et al.* “Uncertainty propagation in nuclear forensics,” *Applied Radiation and Isotopes*, 89, 58-64, (2014).
81. Stanley, Floyd E., *et al.*, “A brief introduction to analytical methods in nuclear forensics,” 295, 1385-1393, (2013).
82. Kemp, R. Scott, *et al.* "[Physical Cryptographic Verification of Nuclear Warheads](#)," *Proceedings of the National Academy of Sciences USA*, 113, (2016).
83. Westgate, John, *et al.*, “Fission-Track Dating,” *Chronometric Dating in Archaeology*, 127-158, (1997).
84. Gleadow, A.J.W. “Fission-track dating methods: What are the real alternatives?,” *Nuclear Tracks*, 5, 1-2, 3-14, (1981).
85. Chung, Brandon, *et al.* “Effects of self-irradiation in plutonium alloys,” *Journal of Nuclear Materials*, 471, (2015).
86. Choudhary, Sumita, *et al.* “Oxidation mechanism of thin Cu films: A gateway towards the formation of single oxide phase” *AIP Advances*, 8, 055114, (2018).
87. Garrison, L.M., *et al.* “The effects of tungsten's pre-irradiation surface condition on helium-irradiated morphology,” *J. Nucl. Mater.*, 466, 302-311, (2015).

88. Zhang, Y., *et al.* “New ion beam materials laboratory for materials modification and irradiation effects research,” *Nuclear Instruments and Methods in Physics*, 338, 19-30, (2014).
89. Crespillo, M.L., *et al.* “Temperature measurements during high flux ion beam irradiations” *Review of Scientific Instruments*, 87, 024902, (2016).
90. Ziegler, J.F., *et al.* “SRIM – The stopping and range of ions in matter,” *Nuclear Instruments and Methods in Physics Research Section B: Beam Interactions with Materials and Atoms*, 268, 11–12, 1818-1823, (2010).
91. Prescher, C., *et al.* “DIOPTAS: a program for reduction of two-dimensional X-ray diffraction data and data exploration,” *High Pressure Research*, 35, 3, 223-230, (2015).
92. Rietveld, H.M., “A profile refinement method for nuclear and magnetic structures,” *Journal of Applied Crystallography*, 2, 2, 65-7, (1969).
93. Toby, B.H., *et al.* “GSAS-II: the genesis of a modern open-source all purpose crystallography software package,” *Journal of Applied Crystallography*, 46, 2, 544-549, (2013).
94. Birtcher, R.C., *et al.* “Damage saturation effects on volume and resistivity changes induced by fission-fragment irradiation of copper,” *Journal of Nuclear Materials*, 98, 1-2, 63-70, (1981).
95. Larson, Bennett C., *et al.* “High-precision measurements of lattice parameter changes in neutron-irradiated copper,” *Journal of Applied Physics*, 45, 514, (1974).
96. English, C.A., *et al.* “Influence of irradiation temperature on self-ion damage in copper,” *Philosophical Magazine*, 34, 4, 603-614, (1976).
97. Daulton, T.L., *et al.* “transmission electron microscopy study in-situ of radiation-induced defects in copper at elevated temperatures,” *Mat. Res. Soc. Symp. Proc.*, 439, (1997).
98. Sun, C., *et al.* “*In situ* study of defect migration kinetics in nanoporous Ag with enhanced radiation tolerance” *Scientific Reports*, 4, 3737, (2014).

99. Pike, Jenna, *et al.* "Formation of stable Cu₂O from reduction of CuO nanoparticles," *Applied Catalysis A: General*, 303, 273-277, (2006).
100. Sander, T., *et al.* "Correlation of intrinsic point defects and the Raman modes of cuprous oxide," *Physical Review B*, 90, 045203, (2014).
- 101 Miranda, R., *et al.* "Invited Review: Influence of ion radiation damage on surface reactivity," *Vacuum*, 34, 12, 1069-1079, (1984).
102. Colas-Leroux, K., *et al.* "Microstructure evolution in ion irradiated oxidized Zircaloy-4 studied with synchrotron radiation micro-diffraction and transmission electron microscopy," *18th International Symposium on Zirconium in the Nuclear Industry*, Hilton Head, United States. ffcea-02438725, (2016).
103. Zhou, Guangwen, *et al.* "Initial oxidation kinetics of copper (110) film investigated by in situ UHV-TEM," *Surface Science*, 531, 359-367, (2003).
104. Bolse, T., *et al.* "Swift heavy ion induced dewetting of metal oxide thin films on silicon," *Nuclear Instruments and Methods in Physics Research B*, 245, 264-268, (2006).
105. Boon, Andries Q.M., *et al.* "Influence of surface oxygen vacancies on the catalytic activity of copper oxide, Part 1: Oxidation of carbon monoxide," *Journal of Molecular Catalysis*, 75, 277-291, (1992).
106. Stratz, S. Adam, *et al.* "Modern Advancements in Post-Detonation Nuclear Forensic Analysis" *International Journal of Nuclear Security*, 2 (3), (2016).
107. Giminaro, Andrew V. *et al.* "Compositional planning for development of synthetic urban nuclear melt glass," *Journal of Radioanalytical Nuclear Chemistry*, 306, 175-181, (2015).
108. Molgaard, Joshua, *et al.* "Development of synthetic nuclear melt glass for forensic analysis," *Journal of Radioanalytical Nuclear Chemistry*, 304, 1293-1301, (2015).

109. Nizinski, Cody A., *et al.* “Production and Characterization of Synthetic Urban Nuclear Melt Glass,” *Journal of Radioanalytical Nuclear Chemistry*, 314, 2349-2355, (2017).
110. Gilbreath, Robert Boone, “Development of Nuclear Underground Engineered Test Surrogates for Technical Nuclear Forensics Exploitation,” *University of Tennessee, Knoxville, Master Theses*, (2017).
111. Seybert, Adam G. *et al.* “Preliminary investigation for the development of surrogate debris from nuclear detonations in marine-urban environments,” *Journal of Radioanalytical Nuclear Chemistry*, 314, 77-85, (2017).
112. National Institute of Standards and Technology, Standard Reference Material 610 website: <https://www-s.nist.gov/srmors/viewTableH.cfm?tableid=90>
113. Hubley, *et al.* “FY18 Year-End Report: Green Chemistry – Dissolution of Post-Detonation Debris with Solid ABF LA-UR-18-30249”
114. Hubley NT, Brockman JD, Robertson JD (2017) Evaluation of ammonium bifluoride fusion for rapid dissolution in post-detonation nuclear forensics analysis. *Radiochim Acta*. 105:629-635.
115. Clegg, Samuel M, *et al.* “Recalibration of the Mars Science Laboratory ChemCam instrument with an expanded geochemical database” *Spectrochimica Acta Part B*, 129, 64-85, (2017).
116. Anderson, Ryan B, *et al.* “Improved accuracy in quantitative laser-induced breakdown spectroscopy using sub-models” *Spectrochimica Acta Part B*, 129, 49-57, (2017).
117. Radboud University, “General Instrumentation: ICP-OES” website: <https://www.ru.nl/science/gi/facilities-activities/elemental-analysis/icp-oes/>

118. Russo, Richard E., et al. "Laser Ablation in Analytical Chemistry" *Analytical Chemistry*, 85, 6162-6177, (2013).
119. Manard, Benjamin T., et al. "Laser ablation - inductively couple plasma - mass spectrometry/laser induced breakdown spectroscopy: a tandem technique for uranium particle characterization" *Journal of Analytical Atomic Spectrometry*, (2017).
120. Krachler, Michael, et al. "Spatial distribution of uranium isotopes in solid nuclear materials using laser ablation multi-collector ICP-MS" *Microchemical Journal*, 140, 24-30, (2018).
121. Clegg, Samuel M., et al. "Multivariate analysis of remote laser-induced breakdown spectroscopy spectra using partial least squares, principal component analysis, and related techniques" *Spectrochimica Acta Part B*, 64, 79-88, (2009).
122. Unnikrishnan, V.K, et al. "Calibration based laser-induced breakdown spectroscopy (LIBS) for quantitative analysis of doped rare earth elements in phosphors" *Materials Letters*, 107, 322-324, (2013).
123. Singh, Manjeet, et al. "Analytical spectral dependent partial least squares regression: a study of nuclear waste glass from thorium based fuel using LIBS" *Journal of Analytical Atomic Spectrometry*, 30, 2507, (2017).
124. Federal Radiation Council, "health implications of fallout from nuclear weapons testing through 1961," 3, (1962).
125. Aarkrog, Asker, "The radiological impact of the Chernobyl debris compared with that from nuclear weapons fallout," *Journal of Environmental Radioactivity*, 6, 2, 151-162, (1988).
126. Stratz, S. Adam, et al. "Modern Advancements in Post-Detonation Nuclear Forensic Analysis" *International Journal of Nuclear Security*, 2 (3), (2016).

127. Massachusetts Institute of Technology, "Spectroscopy History: The Era of Classical Spectroscopy," <http://web.mit.edu/spectroscopy/history/history-classical.html>
128. Rao, Ashwin P., *et al.* "Quantitative Analysis of Cerium-Gallium Alloys Using a Hand-held Laser Induced Breakdown Spectroscopy Device," *Atoms*, 7, 3, 84, (2019).
129. Shattan, Michael B., *et al.* "Mapping of Uranium in Surrogate Nuclear Debris Using Laser-Induced Breakdown Spectroscopy (LIBS)," *Applied Spectroscopy*, 73, 6, 591-600, (2019).
130. Shattan, Michael B., *et al.* "Laser-Induced Plasma Analysis for Surrogate Nuclear Debris," *Journal of Physics: Conference Series*, 1289, 17-22, (2018).
131. Lang, Adam, *et al.* "Analysis of contaminated nuclear plant steel by laser-induced breakdown spectroscopy," *Journal of Hazardous Materials*, 345, 114-122, (2018).
132. Connors, Brendan, *et al.* "Application of Handheld Laser-Induced Breakdown Spectroscopy (LIBS) to Geochemical Analysis," *Applied Spectroscopy*, 70, 810-815, (2016).
133. Anzano, Jesús M., *et al.* "Laser-induced breakdown spectroscopy for quantitative spectrochemical analysis of geological materials: Effects of the matrix and simultaneous determination," *Analytica Chimica Acta*, 575, 2, 230-235, (2006).
134. Rai, Virendra, Thakur, Surya. Physics of Plasma in Laser-Induced Breakdown Spectroscopy 10.1016/B978-044451734-0.50007-7. (2007).].
135. Singh, Manjeet, *et al.* "Analytical spectral dependent partial least squares regression: a study of nuclear waste glass from thorium based fuel using LIBS" *Journal of Analytical Atomic Spectrometry*, 30, 2507, (2017).
136. Unnikrishnan, V.K, *et al.* "Calibration based laser-induced breakdown spectroscopy (LIBS) for quantitative analysis of doped rare earth elements in phosphors" *Materials Letters*, 107, 322-324, (2013).

137. Wold, S. *et al.* "PLS-regression: a basic tool of chemometrics," *Chemom. Intell. Lab. Syst.* 58, 109–130, (2001).
138. Burnham, Alison J., *et al.* "Frameworks for latent variable multivariate regression," *Journal of Chemometrics*, 10, 1, 31-45, (1996).
139. Yeniay, Özgür, *et al.* "A comparison of partial least squares regression with other prediction methods," *Hacettepe Journal of Mathematics and Statistics*, 31, 99-111, (2002).

VITA

Jessica Lyn Bishop was born in Northern Virginia on June 21, 1994. As an undergraduate, she attended Virginia Commonwealth University in Richmond, VA where she graduated with a Bachelor of Science (B.S.) degree in Mechanical and Nuclear Engineering in May 2016. She bicycled across the United States from Yorktown, VA to San Francisco, CA before beginning graduate school at the University of Tennessee in August 2016. She was awarded the Nuclear Energy University Program Graduate Fellowship (\$155,000) in 2017 and she earned her Doctor of Philosophy (Ph.D.) degree in Nuclear Engineering in the Summer of 2020. Through her undergraduate and graduate studies, she has held positions at the International Atomic Energy Agency and Los Alamos National Laboratory where she was able to apply her research towards real life applications.